Strong-coupling theory of bilayer plasmon excitations

Hiroyuki Yamase[1], Luciano Zinni[2], Matías Bejas[3], and Andrés Greco[3]

[1]*Research Center of Materials Nanoarchitectonics (MANA), National Institute for Materials Science (NIMS), Tsukuba 305-0047, Japan*

[2]*Facultad de Ciencias Exactas, Ingeniería y Agrimensura (UNR-CONICET), Avenida Pellegrini 250, 2000 Rosario, Argentina*

[3]*Facultad de Ciencias Exactas, Ingeniería y Agrimensura and Instituto de Física Rosario (UNR-CONICET), Avenida Pellegrini 250, 2000 Rosario, Argentina*

(Dated: October 14, 2025)

Abstract

Recently plasmon excitations in bilayer lattice systems were studied extensively in the weak-coupling regime. Unlike single-layer systems, these bilayers exhibit two distinct modes, $\omega_{\pm}$, which show characteristic dependences upon the momentum and hopping integrals along the z direction. To apply them to cuprates, strong correlation effects should be considered, but a comprehensive analysis has not yet been investigated. In this work, we present a strong-coupling theory to analyze the charge dynamics of a bilayer system, utilizing the t-J-V model, which includes the long-range Coulomb interaction, V, on a lattice. Although our theoretical framework is fundamentally different from the weak-coupling approach, we find that resulting plasmon excitations are similar to those of a weak-coupling theory. A key distinction is that our strong-coupling framework reveals a noticeable suppression of particle-hole excitations, which allows the plasmon modes to remain well-defined over a wider region of momentum. We suggest that the experimentally reported plasmon excitations in Y-based cuprates can be described by the ω_{-} mode, although we call for more systematic experiments to verify this.

I. INTRODUCTION

The parent compounds of cuprate superconductors are widely known to be antiferromagnetic Mott insulators. Upon carrier doping, the charge degrees of freedom become active and the system transitions into a metallic state, which suppresses the antiferromagnetic order. A high-temperature superconducting state emerges at a carrier doping level of approximately 5 % for hole-doped and 10–15 % for electron-doped materials, reaching a maximal T_c around 16 % doping [1].

It is well established that electrons within the CuO_2 layers play a central role in high-temperature superconductivity. For this reason, the two-dimensional t-J and Hubbard models are considered the minimal theoretical framework [2]. While the importance of spin-spin interaction is frequently emphasized, the charge degrees of freedom should be equally crucial to understanding the cuprate physics. The full charge dynamics in momentum-energy space has recently been revealed comprehensively through the advent of the resonant inelastic x-ray scattering (RIXS) technique [3, 4].

In the charge excitation spectrum, two distinct features have been observed. The first feature is low-energy excitations around in-plane momentum $\mathbf{q}_{\parallel} = (0.6\pi, 0)$ in hole-doped cuprates [5–21] and around $(0.5\pi, 0)$ in electron-doped cuprates [22–24]. The second feature is a distinct V-shaped dispersion centered at $\mathbf{q}_{\parallel} = (0, 0)$. While its origin was initially debated [25–30], it is now consistently understood as an acousticlike plasmon, which is a characteristic feature of layered systems [28, 31]. A particular important feature of the plasmon is the rapid decrease of its energy with increasing momentum transfer perpendicular to the layers, q_z [31, 32]. Additionally, a gap at $\mathbf{q}_{\parallel} = (0, 0)$ has been observed [33], which is proportional to the interlayer hopping t_z [28]. This dependence provides a valuable way to extract the value of t_z, a parameter that is difficult to determine through other experimental techniques.

The present paper focuses on the plasmon excitations in cuprate superconductors. While most experimental studies have been limited to single- and infinite-layer systems, where the unit cell contains one CuO_2 plane, a theoretical description requires two additional factors beyond the standard t-J and Hubbard models: the long-range Coulomb interaction (LRC)—which in continuum space has a $1/r$ dependence—and the interlayer hopping, both of which are essential to correctly capture the observed q_z dependence of the plasmon energy

[28, 32, 34].

A crucial theoretical question arises regarding how plasmon excitations change with an increasing number of layers per unit cell. Pioneering studies by Fetter [35] and Griffin and Pindor [36] for a layered electron gas model showed the existence of two modes, one of which has very low energy. Concurrently, the superconducting onset temperature T_c increases substantially when the number of CuO_2 planes is increased to two or three, up to 140 K; for four or more layers, T_c plateaus around 110 K [37].

Experimental studies of low-energy plasmon modes for multilayer cuprates remain limited, with a single report in bilayer Y-based compounds [38]—which has been extensively analyzed within the weak-coupling random phase approximation (RPA) [38–40]—and a subsequent observation in trilayer Bi-based cuprates [41].

The aim of the present work is to formulate a strong-coupling theory for the bilayer system. This work complements the very recent weak-coupling analysis in Ref. [39], allowing us to systematically clarify the similarities and differences between the two theoretical approaches. This point is important because some argue that weak-coupling approaches are inadequate for cuprates, given their strongly correlated nature. In fact, alternative frameworks have been proposed, including holographic descriptions of charge dynamics [42–44]. Furthermore, the formalism developed here acquires renewed relevance following the recent discovery of high-T_c superconductivity in bilayer nickelates [45, 46].

The remainder of this paper is organized as follows. In Sec. II, we formulate a large-N theory of the layered t-J-V model. The LRC is treated on a lattice, respecting the bilayer structure [39], rather than a continuum form used in a layered electron gas model [35, 36]. In Sec. III, we present our results for charge excitation spectra, which may be compared to those obtained in the weak-coupling theory [39]. We also investigate the dependence of these excitation on the LRC, V. Discussions and conclusions are given in Sec. IV and V, respectively. In Appendix A, the complete formalism of our strong coupling theory is presented. In Appendix B, we discuss whether the collective modes obtained within the t-J model without LRC can account for the experimental data.

II. FORMALISM

We begin with our theoretical analysis by defining the bilayer t-J-V model on a square lattice. The Hamiltonian is given by:

$$H = -\sum_{i,j,\sigma,\alpha,\beta} t_{ij}^{\alpha\beta}\tilde{c}_{i\sigma,\alpha}^{\dagger}\tilde{c}_{j\sigma,\beta} - \mu\sum_{i,\alpha} n_{i,\alpha} + J\sum_{\langle i,j\rangle,\alpha}\left(\vec{S}_{i,\alpha}\cdot\vec{S}_{j,\alpha} - \frac{1}{4}n_{i,\alpha}n_{j,\alpha}\right) + \frac{J_{\perp}}{2}\sum_{i,\alpha\neq\beta}\left(\vec{S}_{i,\alpha}\cdot\vec{S}_{i,\beta} - \frac{1}{4}n_{i,\alpha}n_{i,\beta}\right) + \frac{1}{2}\sum_{i\neq j,\alpha,\beta} V_{ij}^{\alpha\beta}n_{i,\alpha}n_{j,\beta}\ , \tag{1}$$

where i and j run over the three-dimensional lattice sites, $\alpha,\beta = 1,2$ denote the plane within a unit cell, and $\tilde{c}_{i\sigma,\alpha}^{\dagger}$ ($\tilde{c}_{i\sigma,\alpha}$) is the creation (annihilation) operator of an electron with spin $\sigma(=\uparrow,\downarrow)$ at site i in layer α. The hopping integrals $t_{ij}^{\alpha\beta}$ extend up to third-nearest neighbors on the square lattice of each layer, denoted as t, t' and t'', respectively. Along the z direction, the hopping within a bilayer is denoted as t_z (intrabilayer hopping), and the hopping between bilayers is given by $t_z^{'}$ (interbilayer hopping)—see Fig. 1. J is the strength of the in-plane spin exchange interaction between nearest-neighbor site $\langle i,j\rangle$; $J_{\perp}$ is the out-of-plane spin exchange and considered only within the intrabilayer; $V_{ij}^{\alpha\beta}$ is the three-dimensional LRC. $n_{i,\alpha} = \sum_{\sigma}\tilde{c}_{i\sigma,\alpha}^{\dagger}\tilde{c}_{i\sigma,\alpha}$ is the electron density operator at site i in layer α, $\vec{S}_{i,\alpha}$ is the spin operator, and μ is the chemical potential. In the t-J-V model, all operators are defined in the Fock space without double occupancy, which yields the local constraint:

$$\sum_{\sigma}\tilde{c}_{i\sigma,\alpha}^{\dagger}\tilde{c}_{i\sigma,\alpha} \leq 1 \tag{2}$$

for any site i and layer α.

Here we employ a large-N technique in a path integral formalism in terms of the Hubbard operators [47]. In this scheme, the number of spin component is extended from 2 to N and physical quantities are computed by the power of $1/N$ systematically.

Setting $t_z = t_z^{'} = J_{\perp} = V_{ij}^{\alpha\beta} = 0\,(\alpha\neq\beta)$ in Eq. (1) reduces the system to two decoupled t-J-V models. Such a model was successfully applied to analyzing the charge dynamics in cuprates [28, 32–34, 48–51]. We extend this formalism to the bilayer lattice shown in Fig. 1, which was originally introduced to analyze bilayer nickelates [52]. Our interest lies in bilayer plasmon excitations and we now summarize the key steps of this formalism. The complete formalism is given in Appendix A.

At leading order in the bilayer system, the electron Green's function is obtained as 2×2

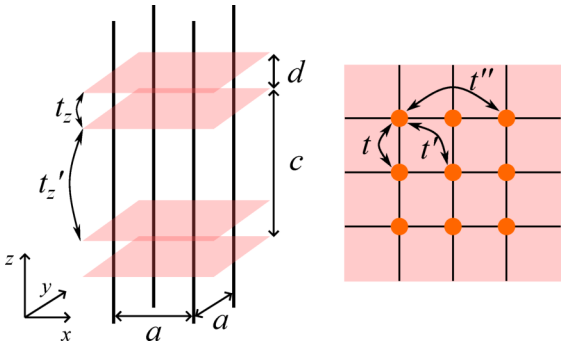

FIG. 1. Schematic of the bilayer lattice and corresponding hopping integrals. Each layer forms a square lattice with lattice constant a; d is the intrabilayer distance and c is the lattice constant along the z direction.

matrix:

$$G^{(0)}_{\alpha\beta}(\mathbf{k}, \mathrm{i}\nu_n) = \begin{pmatrix} \mathrm{i}\nu_n - \varepsilon^{\parallel}_{\mathbf{k}} & -\varepsilon^{\perp}_{\mathbf{k}} \mathrm{e}^{\mathrm{i}k_z \frac{d}{c}} \\ -\varepsilon^{\perp *}_{\mathbf{k}} \mathrm{e}^{-\mathrm{i}k_z \frac{d}{c}} & \mathrm{i}\nu_n - \varepsilon^{\parallel}_{\mathbf{k}} \end{pmatrix}^{-1} , \tag{3}$$

where ν_n is a fermionic Matsubara frequency, and the electron dispersions are obtained as

$$\varepsilon^{\parallel}_{\mathbf{k}} = -2\left(t\frac{\delta}{2} + \chi\right)(\cos k_x + \cos k_y) - 4t'\frac{\delta}{2}\cos k_x \cos k_y - 2t''\frac{\delta}{2}(\cos 2k_x + \cos 2k_y) - \mu\,, \tag{4}$$

$$\varepsilon^{\perp}_{\mathbf{k}} = -\left[t_z\frac{\delta}{2}(\cos k_x - \cos k_y)^2 + \chi'\right] - t_z'\frac{\delta}{2}(\cos k_x - \cos k_y)^2\,\mathrm{e}^{-\mathrm{i}k_z}\,. \tag{5}$$

Here k_x, k_y and k_z are in units of the inverse of the lattice constant a, a, and c, respectively. For a given doping δ, the chemical potential μ and the values χ and χ' are determined self-consistently by solving:

$$\chi = \frac{J}{8N_s}\sum_{\mathbf{k}}(\cos k_x + \cos k_y)\left[n_F(\varepsilon^1_{\mathbf{k}}) + n_F(\varepsilon^2_{\mathbf{k}})\right]\,, \tag{6}$$

$$\chi' = -\frac{J_\perp}{4N_s}\sum_{\mathbf{k}}\frac{\varepsilon^{\perp}_{\mathbf{k}}\mathrm{e}^{\mathrm{i}k_z\frac{d}{c}}}{|\varepsilon^{\perp}_{\mathbf{k}}|}\left[n_F(\varepsilon^1_{\mathbf{k}}) - n_F(\varepsilon^2_{\mathbf{k}})\right]\,, \tag{7}$$

and

$$1 - \delta = \frac{1}{N_s}\sum_{\mathbf{k}}\left[n_F(\varepsilon^1_{\mathbf{k}}) + n_F(\varepsilon^2_{\mathbf{k}})\right]\,, \tag{8}$$

where N_s is the number of lattice sites; n_F is the Fermi distribution function; from the determinant of Eq. (3), the bonding and antibonding bands ($\alpha = 1, 2$, respectively) can be obtained as

$$\varepsilon^{\alpha}_{\mathbf{k}} = \varepsilon^{\parallel}_{\mathbf{k}} - (-1)^{\alpha}|\varepsilon^{\perp}_{\mathbf{k}}|\,. \tag{9}$$

Charge fluctuations are described by the 14×14 matrix of the boson propagator at the order of the $1/N$ in the bilayer system. But the on-site charge fluctuations including plasmons that we are interested in are described by a 4×4 reduced matrix,

$$D_{ab}^{-1}(\mathbf{q}, \mathrm{i}\omega_n) = \left[D_{ab}^{(0)}(\mathbf{q}, \mathrm{i}\omega_n)\right]^{-1} - \Pi_{ab}(\mathbf{q}, \mathrm{i}\omega_n)\,, \tag{10}$$

where a and b run from 1 to 4; $\mathbf{q}$ is a three-dimensional vector; ω_n is a bosonic Matsubara frequency. $D_{ab}^{(0)}(\mathbf{q}, \mathrm{i}\omega_n)$ is the bare bosonic propagator and is obtained as

$$\left[D_{ab}^{(0)}(\mathbf{q}, \mathrm{i}\omega_n)\right]^{-1} = N \begin{pmatrix} \frac{\delta^2}{2}\left[\frac{V(\mathbf{q})}{2} - J(\mathbf{q})\right] & \frac{\delta}{2} & \frac{\delta^2}{2}\left[\frac{V'(\mathbf{q})}{2} - J'(\mathbf{q})\right] & 0 \\ \frac{\delta}{2} & 0 & 0 & 0 \\ \frac{\delta^2}{2}\left[\frac{V'^*(\mathbf{q})}{2} - J'^*(\mathbf{q})\right] & 0 & \frac{\delta^2}{2}\left[\frac{V(\mathbf{q})}{2} - J(\mathbf{q})\right] & \frac{\delta}{2} \\ 0 & 0 & \frac{\delta}{2} & 0 \end{pmatrix}, \tag{11}$$

where $J(\mathbf{q}) = (J/2)(\cos q_x + \cos q_y)$ (q_x and q_y are in units of the inverse of the lattice constant a) and $J'(\mathbf{q}) = (J_\perp/4)\mathrm{e}^{-\mathrm{i}q_z\frac{d}{c}}$ (q_z is in units of the inverse of the lattice constant c). $V(\mathbf{q})$ and $V'(\mathbf{q})$ are the intralayer and interlayer Fourier components of the LRC in the bilayer lattice, respectively, which are given by

$$V(\mathbf{q}) = \frac{V_c}{\det\tilde{V}}\left[\alpha\left(2 - \cos q_x - \cos q_y\right) - \frac{1}{2}h_3 - \frac{1}{2}h_1\cos q_z\right]\,, \tag{12}$$

$$\begin{aligned} V'(\mathbf{q}) =& \frac{1}{2}\frac{V_c}{\det\tilde{V}}\left\{h_2\cos\left(q_z\frac{d}{c}\right) + h_4\cos\left[q_z\left(1 - \frac{d}{c}\right)\right] - \mathrm{i}h_2\sin\left(q_z\frac{d}{c}\right)\right. \\ & \left. +\mathrm{i}h_4\sin\left[q_z\left(1 - \frac{d}{c}\right)\right]\right\}\,, \end{aligned} \tag{13}$$

$$\begin{aligned} \det\tilde{V} =& \left[\alpha\left(2 - \cos q_x - \cos q_y\right)\right]^2 - \alpha\left(2 - \cos q_x - \cos q_y\right)\left(h_1\cos q_z + h_3\right) \\ & + \frac{6c^2}{(c-d)(2c-d)}\left(1 - \cos q_z\right)\,. \end{aligned} \tag{14}$$

Here $V_c = \frac{e^2 c}{2a^2\varepsilon_\perp}$, $\alpha = \frac{c^2\varepsilon_\parallel}{a^2\varepsilon_\perp}$ ($\varepsilon_\parallel$ and $\varepsilon_\perp$ are the parallel and perpendicular dielectric constants, respectively; e is the electric charge of electron), and $h_1 = \frac{2c(c-2d)}{(2c-d)(c-d)}$, $h_2 = \frac{2c}{c-d}$, $h_3 = -\frac{4c}{c-d}$, and $h_4 = \frac{2c(c+d)}{(2c-d)(c-d)}$. Equations (12) and (13) were first derived in Ref. [39] and they represent the only known analytical expressions for the LRC in the bilayer structure. The self-energy components $\Pi_{ab}(\mathbf{q}, \mathrm{i}\omega_n)$ in Eq. (10) are calculated in Appendix A.

In the large-N formalism for bilayer systems, the charge-charge correlation function $\chi(\mathrm{r}_i - \mathrm{r}_j, \tau) = \langle T_\tau n_i(\tau) n_j(0)\rangle$ is related in $\mathbf{q}$-ω space to the dressed bosonic propagator $D_{ab}(\mathbf{q}, \mathrm{i}\omega_n)$ as

$$\chi\left(\mathbf{q}, \mathrm{i}\omega_n\right) = \frac{N}{2}\left(\frac{\delta}{2}\right)^2\left[D_{11}\left(\mathbf{q}, \mathrm{i}\omega_n\right) + D_{33}\left(\mathbf{q}, \mathrm{i}\omega_n\right) + D_{13}\left(\mathbf{q}, \mathrm{i}\omega_n\right) + D_{31}\left(\mathbf{q}, \mathrm{i}\omega_n\right)\right]\,. \tag{15}$$

The elements D_{11} and D_{33} (D_{13} and D_{31}) give the intralayer (interlayer) contributions to $\chi(\mathbf{q}, \mathrm{i}\omega_n)$.

After performing the analytical continuation $\mathrm{i}\omega_n \to \omega + \mathrm{i}\Gamma$ and adopting the physical value $N = 2$, we obtain the imaginary part of the charge-charge correlation function, $\mathrm{Im}\chi(\mathbf{q}, \omega)$, which can be directly compared with RIXS measurements. The parameter Γ may account for both experimental resolution and spectral broadening from electron correlations [53].

III. RESULTS

We present our results organized into three subsection. Focusing on cuprates, we adopt the following parameter set without losing generality: $t' = -0.3t$, $t'' = 0.15t$, $J = 0.3t$, $J_\perp = 0$ [54]. The lattice parameters are set to $a = 3.88$ Å, $c = 11.68$ Å, $d = 3.36$ Å[38]. The dielectric constants are chosen as $\epsilon_\parallel = 6\epsilon_0$, $\epsilon_\perp = 2.25\epsilon_0$. These values yield $V_c = 38.75t$ and $\alpha = 24$. We take hole doping rate $\delta = 0.21$, corresponding to the electron density $n = 0.79$. The broadening parameter Γ is set to $0.01t$ except for Fig. 12. We take a temperature of $T = 0.04t$ to avoid bond-charge instabilities [55, 56]. Our analysis first focuses on the case of $t_z^{'} = 0$ before examining its effect. Unless stated otherwise, t is the unit of energy.

A. Charge excitation spectra with $t_z^{'} = 0$

1. *Overall spectrum*

Figure 2(a) presents the charge excitations spectrum across a broad range of in-plane momentum $\mathbf{q}_\parallel$ and energy transfer ω. The white dotted curve shows the upper boundary of the particle-hole continuum. While weak signals are visible below this boundary, the most significant spectral weight is found above it, corresponding to plasmon excitations. These features are qualitatively similar to those observed in a single-layer system (see Fig. 1 in Ref. [28]). A crucial distinction emerges at low energy ($\omega < 0.3t$) and small in-plane momentum, specifically around $\mathbf{q}_\parallel = (0, 0)$, where two distinct plasmon modes are present for a fixed $q_z = \pi$. Upon closer inspection, the lower branch is found to be a gapless plasmon mode that extends into the continuum, a feature characteristic of bilayer systems [39]. Following the nomenclature of Griffin and Pindor [36], we refer to the higher-energy and lower-energy branches as ω_+ and ω_- modes, respectively.

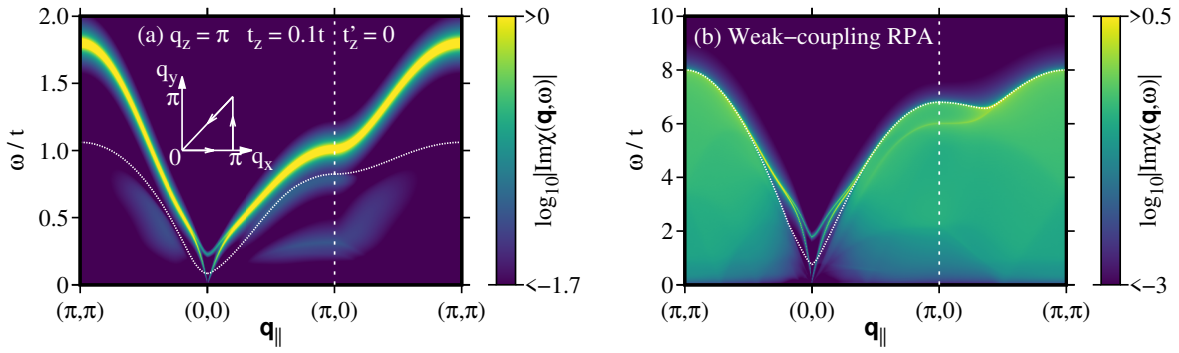

FIG. 2. (a) Intensity map of charge excitation spectrum $\log_{10}|\mathrm{Im}\chi(\mathbf{q},\omega)|$ in the plane of in-plane momentum $\mathbf{q}_\parallel$ and energy transfer ω. The white dotted curve represents the upper boundary of the particle-hole continuum excitations. The strong intensity corresponds to plasmon modes. (b) The corresponding map in a weak-coupling analysis [39] for the same parameters as (a) except that $V_c = 130$ is taken.

The corresponding weak-coupling RPA result [39] is shown in Fig. 2(b) for exactly the same parameters as Fig. 2(a) except for a value of V_c so that two plasmon branches are well visible. A comparison between Fig. 2(a) and (b) reveals that strong electronic correlations suppress the particle-hole continuum substantially, allowing the plasmon branches to remain well defined along the entire Brillouin-zone path, whereas in the weak-coupling scheme they are confined to the vicinity of $\mathbf{q}_\parallel = (0,0)$ and merge into the continuum away from $\mathbf{q}_\parallel = (0,0)$.

The remainder of this section will focus on the detailed properties of ω_+ and ω_- modes.

2. Plasmon excitations

To investigate the plasmon excitations in more detail, we analyze the $\mathbf{q}$-ω map around $\mathbf{q}_\parallel = (0,0)$ for a sequence of q_z values as shown in Figs. 3(a)–(e). At $q_z = 0$ [Fig. 3(a)], only the ω_+ mode is present. The charge conservation makes the spectral weight vanish at $\mathbf{q}_\parallel = (0,0)$ because charge fluctuations between the two layers are in-phase. This confirms that the ω_+ mode corresponds to the well-known optical plasmon. By symmetry, the ω_- mode corresponds to out-of-phase fluctuations and is not present for $q_z = 0$, a feature that has the following physical interpretation: When applying infinitesimally small external

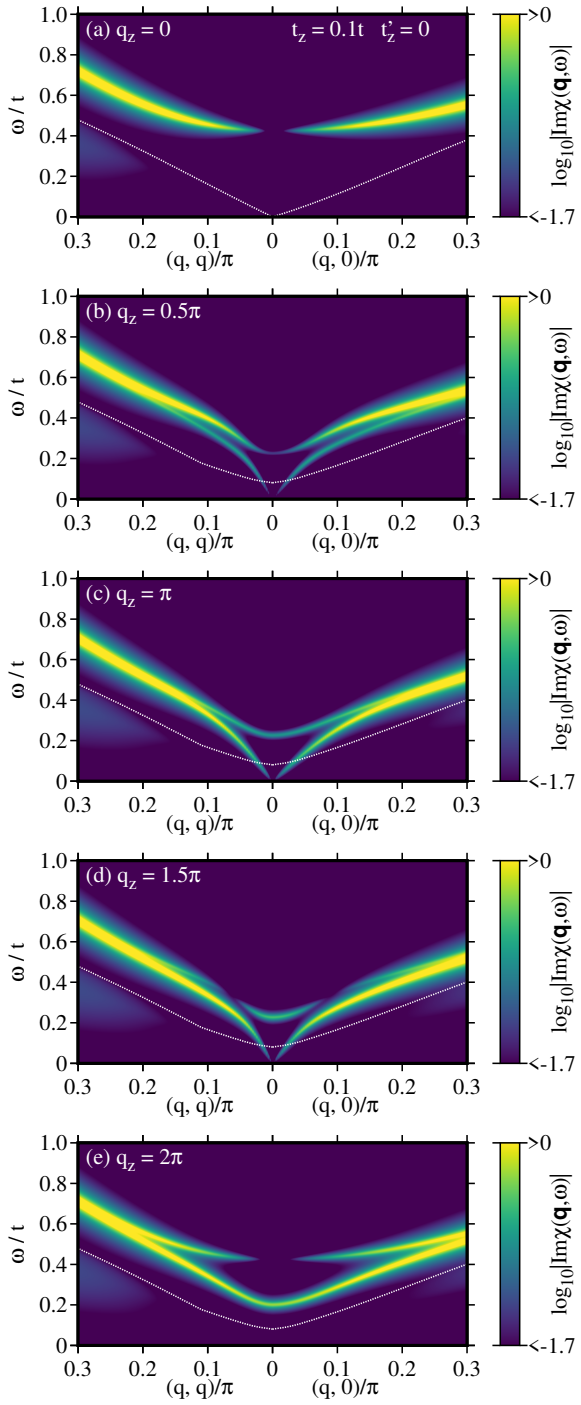

FIG. 3. Intensity maps of $\log_{10}|\mathrm{Im}\chi(\mathbf{q},\omega)|$ for a sequence of q_z around a region of $\mathbf{q}_{\parallel} = (0,0)$ for $t_z = 0.1t$: (a) $q_z = 0$, (b) $q_z = 0.5\pi$, (c) $q_z = \pi$, (d) $q_z = 1.5\pi$, and (e) $q_z = 2\pi$. The white dotted curve denotes the upper boundary of the particle-hole continuum. It goes to zero at $\mathbf{q}_{\parallel} = (0,0)$ and $q_z = 0$ in (a).

electric field with $q_z = 0$, this external field is strictly uniform along the out-of-plane direction

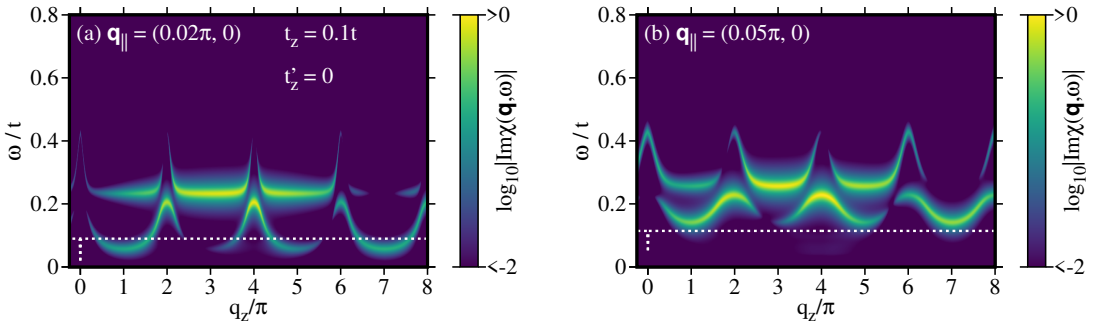

FIG. 4. q_z dependence of ω_+ mode (higher energy) and ω_- mode (lower energy) at (a) $\mathbf{q}_\parallel = (0.02\pi, 0)$ and (b) $\mathbf{q}_\parallel = (0.05\pi, 0)$ for $t_z = 0.1t$. The white dotted line is the upper boundary of the continuum spectrum and exhibits a sharp drop at $q_z = 0$ because of the vanishing of the ω_- mode there.

and thus cannot couple to the out-of-phase charge oscillation, i.e., ω_- mode.

Although the spectral weight at $\mathbf{q}_\parallel = (0, 0)$ vanishes for $q_z = 0$, a finite intrabilayer hopping t_z results in a finite energy for the upper boundary of the continuum at $\mathbf{q}_\parallel = (0, 0)$ for $q_z \neq 0$. This allows for the presence of two plasmon modes, the ω_+ and ω_- modes, as seen in Figs. 3(b)–(d). These modes should not be confused with the even and odd modes, since the LRC couples fluctuations across all layers. Notably, the ω_- mode exhibits a gapless dispersion, which is particularly evident as it enters the continuum around $\mathbf{q}_\parallel = (0, 0)$. However, a significant change occurs at $q_z = 2n\pi$ where $n \neq 0$ [Fig. 3(e)], as the ω_- mode becomes gapped. A comparison between Figs. 3(a) and (e) reveals that the plasmon excitations at $q_z = 0$ are not generic. Instead, the behavior at $q_z = 2n\pi$ with $n \neq 0$ is more representative: both $\omega_\pm$ modes are present and gapped, but the intensity of the ω_+ mode vanishes at $\mathbf{q}_\parallel = (0, 0)$ while it does not for the ω_- mode.

We next examine the q_z dependence of the $\omega_\pm$ modes more closely. Figure 4(a) shows results at a fixed in-plane momentum of $\mathbf{q}_\parallel = (0.02\pi, 0)$ for $t_z = 0.1t$. The white dotted line indicates the upper boundary of the particle-hole continuum. The ω_+ mode is always present above the continuum. Its energy sharply peaks at $q_z = 2n\pi$ (corresponding to the optical plasmon) and quickly decreases as q_z moves away from these values, remaining largely q_z independent until the next peak. The ω_- mode, which is absent at $q_z = 0$, gains intensity immediately as q_z increases. It shows a dispersive feature between $\omega = 0.06$–$0.21t$ with a peak at $q_z = 2n\pi$ where $n \neq 0$. This dispersion is particularly interesting since it occurs by

crossing the boundary of the continuum.

Figure 4(b) presents the same plot but for slightly larger in-plane momentum $\mathbf{q}_\parallel = (0.05\pi, 0)$. The ω_+ mode exhibits a q_z dependence similar to that in Fig. 4(a). The ω_- mode, however, shows a clear cosinelike dispersion along the q_z direction and is situated entirely above the continuum.

In both Figs. 4(a) and (b), the intensity of the $\omega_\pm$ modes displays a characteristic q_z dependence, with "nodes" where the spectral weight almost vanishes at specific q_z values. For example, the ω_+ mode loses intensity around $q_z = 7\pi$. These positions are parameter dependent, especially on the ratio of d/c, though the vanishing intensity of the ω_- mode at $q_z = 0$ is a robust feature. It is also important to note that the intensity of both $\omega_\pm$ modes does not have 2π periodicity along the q_z direction.

For completeness, we also investigate the case of a large intrabilayer hopping $t_z = 0.3t$. The spectral maps for various q_z are shown in Fig. 5. Similar to the $t_z = 0.1t$ case, only a single mode is present at $q_z = 0$ [Fig. 5(a)], and its vanishing spectral weight at $\mathbf{q}_\parallel = (0, 0)$ identifies it as the ω_+ mode. For $q_z \neq 0$ [Figs. 5(b)–(d)], two modes appear. A remarkable feature in this large t_z case is that the upper mode forms an upward-convex shape around $\mathbf{q}_\parallel = (0, 0)$ whereas the other mode is gapless and sharply defined even inside the continuum. At $q_z = 2\pi$ [Fig. 5(e)], two gapped modes are present. However, a key difference from the $t_z = 0.1t$ case is that the lower-energy mode in Fig. 5(e) is the one with zero spectral weight at $\mathbf{q}_\parallel = (0, 0)$, identifying it as the ω_+ mode. Given the continuity of the modes with varying q_z, this suggests a reversal in the energy hierarchy of the $\omega_\pm$ modes for a large t_z. Specifically the ω_+ mode becomes gapless for $q_z \neq 2n\pi$, while ω_- mode is always gapped except for its vanishing at $q_z = 0$. This inversion can be traced back to the competing energy scales set by the LRC—through V_c and α—and by the intrabilayer hopping t_z. When t_z becomes sufficiently large, the energy scale of the ω_- mode can exceed the optical plasmon energy at $q_z = 2n\pi$, producing the observed reversal between the ω_+ and ω_- modes. This situation can be realized for a system with a smaller intrabilayer distance. Designing materials in this way would be highly interesting.

As we observed in Fig. 5, the ω_- mode has higher energy than the ω_+ mode for large t_z. This is confirmed by the results in Figs. 6(a) and (b), where the higher-energy mode shows zero spectral weight at $q_z = 0$, characteristic of the ω_- mode. The q_z dependence of the ω_- mode for large t_z is markedly different from the $t_z = 0.1t$ case, showing a dip rather

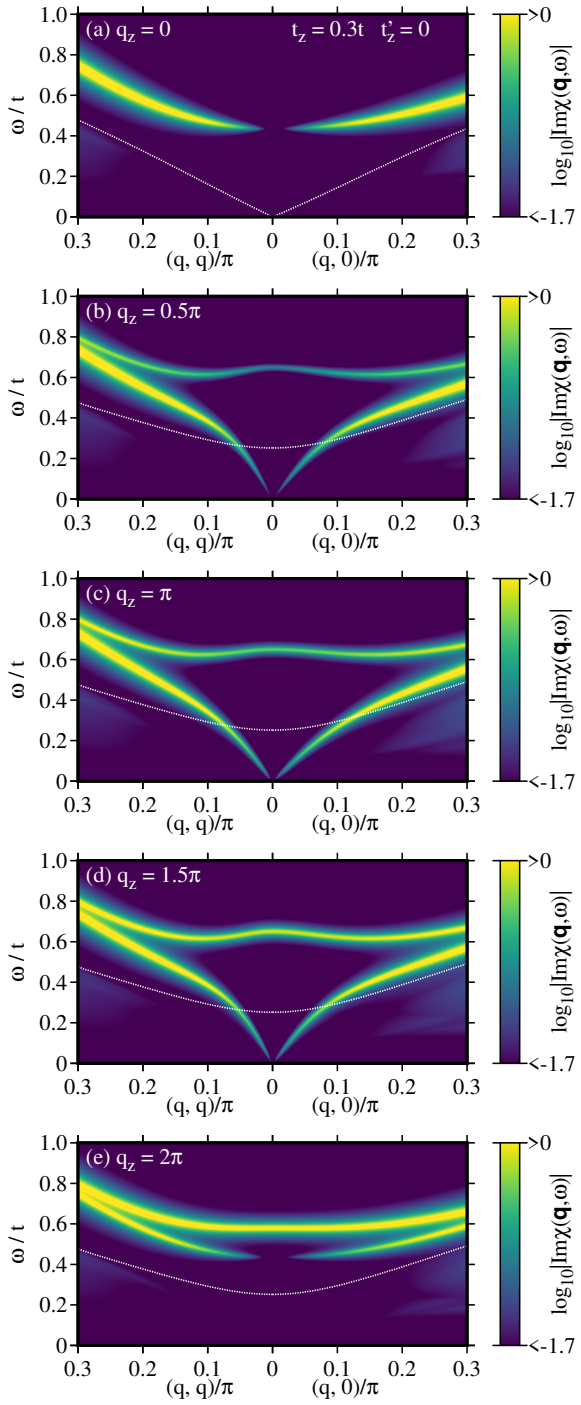

FIG. 5. Intensity maps of $\log_{10}|\mathrm{Im}\chi(\mathbf{q},\omega)|$ for a sequence of q_z around a region of $\mathbf{q}_{\parallel} = (0,0)$ for $t_z = 0.3t$: (a) $q_z = 0$, (b) $q_z = 0.5\pi$, (c) $q_z = \pi$, (d) $q_z = 1.5\pi$, and (e) $q_z = 2\pi$. The white dotted curve denotes the upper boundary of the particle-hole continuum. It becomes zero at $\mathbf{q}_{\parallel} = (0,0)$ and $q_z = 0$ in (a).

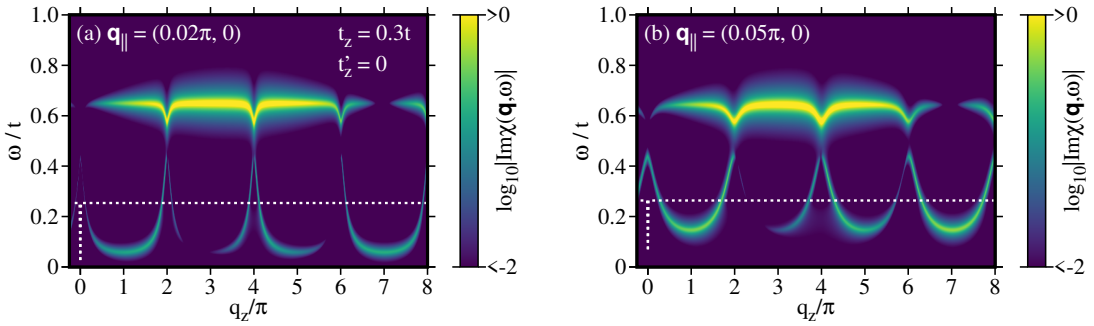

FIG. 6. q_z dependence of ω_+ mode (lower energy) and ω_- mode (higher energy) at (a) $\mathbf{q}_\parallel = (0.02\pi, 0)$ and (b) $\mathbf{q}_\parallel = (0.05\pi, 0)$ for $t_z = 0.3t$. The corresponding results of $t_z = 0.1t$ are shown in Fig. 4. The white dotted line is the upper boundary of the continuum spectrum and exhibits a sharp drop at $q_z = 0$ because of the vanishing of the ω_- mode there.

than a peak at $q_z = 2n\pi$. In contrast, the low-energy ω_+ mode exhibits a significant dispersive feature, particularly at $\mathbf{q}_\parallel = (0.02\pi, 0)$, where its energy spans a wide range between $\omega = 0.06$–$0.44t$. This mode is sharply defined even when it lies within the continuum, a consequence of the very low spectral weight of the continuum itself near $\mathbf{q}_\parallel = (0, 0)$. At $\mathbf{q}_\parallel = (0.05\pi, 0)$ shown in Fig. 6(b), the ω_+ mode is less dispersive, but shows a similar overall feature.

B. Charge excitation spectra with $t_z' \neq 0$

The previous analysis has focused on the case of zero interbilayer hopping ($t_z' = 0$), though the LRC is included. Here, we extend our study to investigate the effect of a finite t_z'. We begin by assuming a moderate value of $t_z' = t_z/2 = 0.05t$ and later present results for a larger t_z' to capture the behavior observed for a large t_z in the previous subsection.

We present results in a manner consistent with Figs. 3(a)–(e), as shown in Figs. 7(a)–(e). At $q_z = 0$ [Fig. 7(a)], the spectrum is nearly identical to the $t_z' = 0$ case in Fig. 3(a), with only the ω_+ mode present. This indicates that the effect of t_z' is negligible at $q_z = 0$. A similar minor effect is seen at $q_z = 2\pi$ [Fig. 7(e)], where the ω_- mode exists and is shifted to a slightly higher energy due to the inclusion of t_z'. The most significant change induced by a finite t_z' is observed at $q_z \neq 2n\pi$, where the ω_- mode, which was gapless for $t_z' = 0$, now becomes gapped at $\mathbf{q}_\parallel = (0, 0)$. Consequently, for any $q_z \neq 0$, we have two gapped plasmon

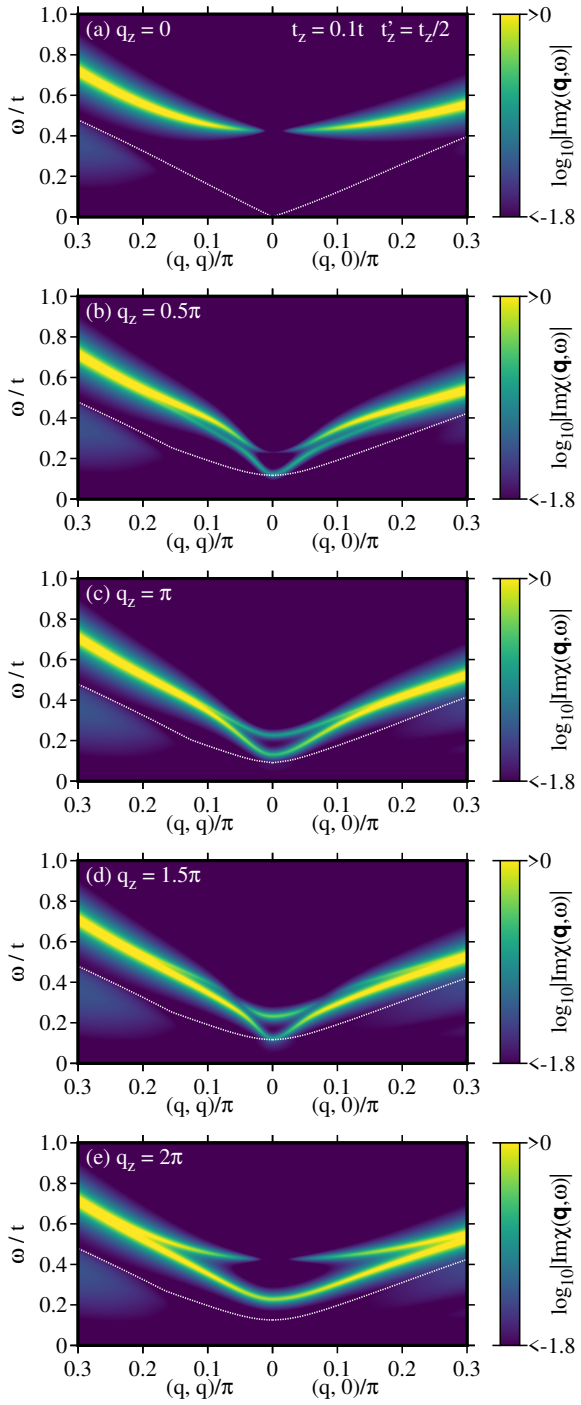

FIG. 7. Intensity maps of $\log_{10}|\mathrm{Im}\chi(\mathbf{q},\omega)|$ for a sequence of q_z around a region of $\mathbf{q}_{\parallel} = (0,0)$ for $t_z = 0.1t$ and $t_z^{'} = t_z/2$: (a) $q_z = 0$, (b) $q_z = 0.5\pi$, (c) $q_z = \pi$, (d) $q_z = 1.5\pi$, and (e) $q_z = 2\pi$. The white dotted curve denotes the upper boundary of the particle-hole continuum. There is no continuum spectrum at $\mathbf{q}_{\parallel} = (0,0)$ and $q_z = 0$.

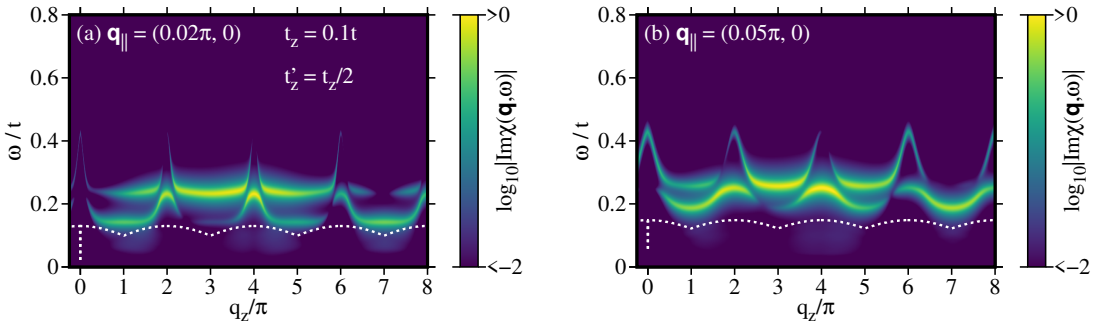

FIG. 8. q_z dependence of ω_+ mode (higher energy) and ω_- mode (lower energy) at (a) $\mathbf{q}_\parallel = (0.02\pi, 0)$ and (b) $\mathbf{q}_\parallel = (0.05\pi, 0)$ for $t_z = 0.1t$ and $t_z^{'} = t_z/2$. The white dotted curve denotes the upper boundary of the particle-hole continuum. There is a sharp drop at $q_z = 0$ because of the disappearance of the ω_- mode there.

modes in the presence of $t_z^{'}$.

The q_z dependence of the $\omega_\pm$ modes is presented in Figs. 8(a) and (b) for $\mathbf{q}_\parallel = (0.02\pi, 0)$ and $(0.05\pi, 0)$, respectively. A comparison with Figs. 4(a) and (b) shows that the overall behavior is preserved, with the primary difference being a shift of the ω_- mode to higher energy due to the finite $t_z^{'}$. While the spectral intensity does not exhibit 2π periodicity, the location of the "nodes", where the intensity is strongly suppressed, remain largely unaffected by the inclusion of $t_z^{'}$. This suggests that the effect of $t_z^{'}$ is relatively weak on the intensity dependence of the plasmon modes.

For completeness, we also study the case of a large hopping $t_z = 0.3t$ with $t_z^{'} = 0.15t$. As we have previously established, the energy hierarchy of the $\omega_\pm$ modes is interchanged for a large t_z, and this behavior persists in the presence of $t_z^{'}$.

q-ω maps for this case are shown in Figs. 9(a)–(e). At $q_z = 0$ [Fig. 9(a)], only the ω_+ mode is present, with its spectral weight vanishing at $\mathbf{q}_\parallel = (0, 0)$ as a consequence of charge conservation. For $q_z \neq 0$, the particle-hole continuum gains spectral weight even at $\mathbf{q}_\parallel = (0, 0)$, and the ω_+ mode is realized close to this upper boundary around $\mathbf{q}_\parallel = (0, 0)$. In contrast, the ω_- mode has a higher energy and is located above the continuum. As seen in Fig. 9(b), the ω_- mode has a relatively low-spectral weight near $q_z = 0$ and forms an upward-convex shape centered at $\mathbf{q}_\parallel = (0, 0)$ and $\omega \approx 0.65t$. This mode gains more spectral weight as q_z increases as shown in Figs. 9(c)–(e), and its dispersion shows a small dependence on q_z. The low-energy ω_+ mode enters slightly the continuum around $\mathbf{q} = (0, 0)$ in Figs. 9(b)

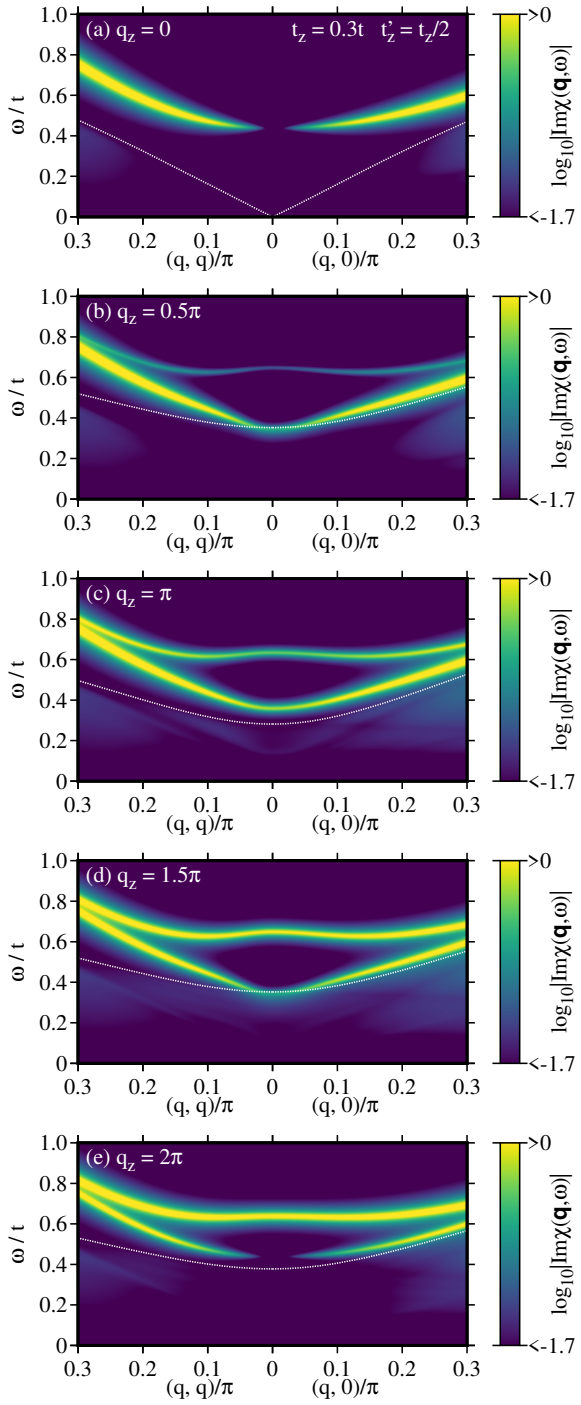

FIG. 9. Intensity maps of $\log_{10}|\mathrm{Im}\chi(\mathbf{q},\omega)|$ in the presence of a large $t_z = 0.3t$ and $t'_z = t_z/2$. (a)–(e) $\mathbf{q}_{\parallel}$ dependence for a sequence of q_z around a region of $\mathbf{q}_{\parallel} = (0,0)$: (a) $q_z = 0$, (b) $q_z = 0.5\pi$, (c) $q_z = \pi$, (d) $q_z = 1.5\pi$, and (e) $q_z = 2\pi$. The white dotted curve denotes the upper boundary of the particle-hole continuum—there is no continuum spectrum at $\mathbf{q}_{\parallel} = (0,0)$ and $q_z = 0$ in (a).

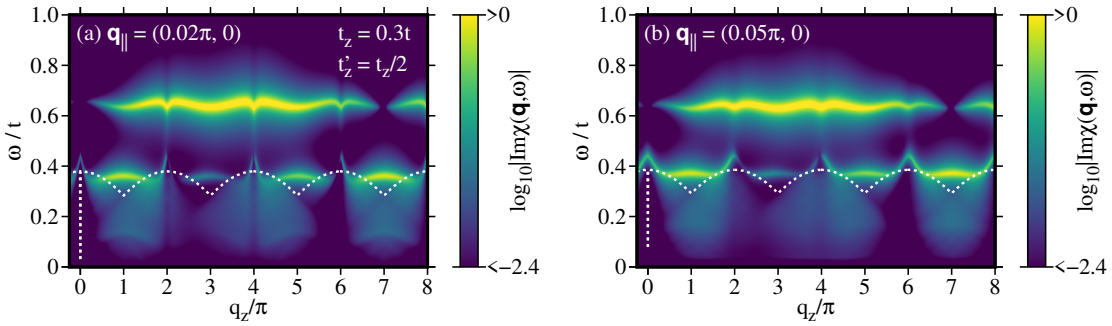

FIG. 10. q_z dependence of ω_+ mode (lower energy) and ω_- mode (higher energy) at (a) $\mathbf{q}_\parallel = (0.02\pi, 0)$ and (b) $\mathbf{q}_\parallel = (0.05\pi, 0)$ for $t_z = 0.3t$ and $t_z' = t_z/2$. The white dotted curve denotes the upper boundary of the particle-hole continuum. There is a sharp drop at $q_z = 0$ because of the disappearance of the ω_- mode there.

and (d). Its presence, despite being within the continuum, is due to the low-spectral weight of the continuum around $\mathbf{q}_\parallel = (0, 0)$. At $q_z = 2\pi$ [Fig. 9(e)], the ω_+ mode is pushed up slightly above the continuum and its spectral intensity at $\mathbf{q}_\parallel = (0, 0)$ vanishes.

Finally, we examine the q_z dependence of the spectral intensity at fixed in-plane momenta in Figs. 10(a) and (b) for $\mathbf{q}_\parallel = (0.02\pi, 0)$ and $(0.05\pi, 0)$, respectively. The ω_+ mode is well defined when it is located above the continuum, and is somewhat blurred within the continuum, but a sharp peak is discernible at $q_z = 2n\pi$, particularly in Fig. 10(b). The ω_- mode, which vanishes at $q_z = 0$, exhibits a less dispersive feature along the q_z direction, with a small dip at $q_z = 2n\pi$ $(n \neq 0)$. The strong suppression of the ω_- mode around $q_z = 7\pi$ is a feature also observed in the previous subsection.

C. V_c dependence of dispersive modes

The t-J-V model contains a short-range interaction of the J-term as well as from the local constraint, and thus we can study the interplay with the long-range interaction V.

In the case of $q_z = 0$, we have only the ω_+ mode with a gap [Fig. 3(a)]. This mode eventually becomes a gapless mode in the limit of $V_c \to 0$, forming the zero-sound mode, as shown in Fig. 11, although the mode along the q_x direction is realized very close to the upper boundary of the continuum in Fig. 11(b).

At $q_z = \pi$, both ω_+ and ω_- modes are present, with the ω_- mode being gapless as shown

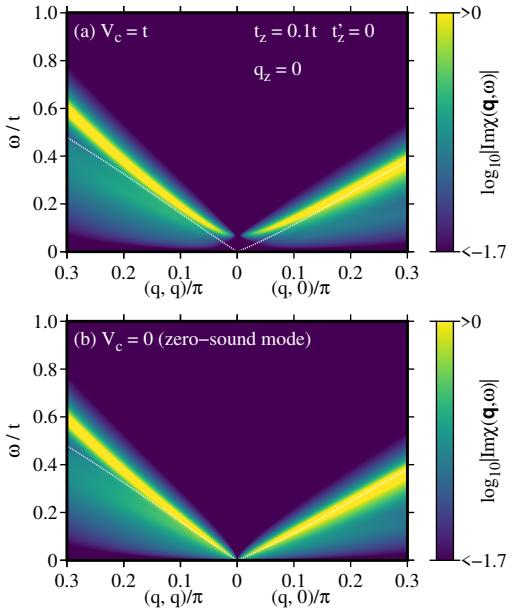

FIG. 11. Forming the zero-sound mode in the limit of $V_c \to 0$: (a) $V_c = t$ and (b) $V_c = 0$. It is the ω_+ mode that changes into the zero-sound mode.

in Fig. 12(a). As the interaction strength V_c is reduced, the energy of the ω_+ mode decreases, but it remains a gapped mode in the limit of $V_c \to 0$. In contrast, the ω_- mode retains its gapless character, though the velocity is reduced as V_c decreases. While it might appear that plasmon modes persist in the $V_c = 0$ limit, they are no longer plasmons. In particular, the ω_- mode is realized inside the continuum as a peak of the continuum. On the other hand, if we include t_z', both $\omega_\pm$ modes are gapped even in the limit of $V_c \to 0$.

A unique feature is observed at $q_z = 2n\pi$. As previously shown in Fig. 3(e) both $\omega_\pm$ modes are gapped when $n \neq 0$. As V_c decreases [Fig. 12(b)], this gap is reduced. In contrast to the case of $q_z = 0$ [Fig. 11(b)], the ω_+ mode retains a gap in the limit of $V_c \to 0$. In this limit, it is the ω_- mode that changes into a gapless mode, namely evolves into the zero-sound-wavelike mode. This feature is the same even if there is a finite t_z'.

Corresponding spectra showing the q_z dependence at $\mathbf{q}_\parallel = (0.05\pi, 0)$ are presented in Fig. 13 in the limit of $V_c = 0$, where there are two branches. The analysis of this figure provides three important insights. First, while the lower-energy branch at $q_z = 0$ is the zero-sound mode, it smoothly connects to a branch at a finite q_z. Second, because the V-term is the primary source of three-dimensional coupling, the system effectively reduces to being two-dimensional in the $V_c = 0$ limit, resulting in a very weak dependence on q_z. Third,

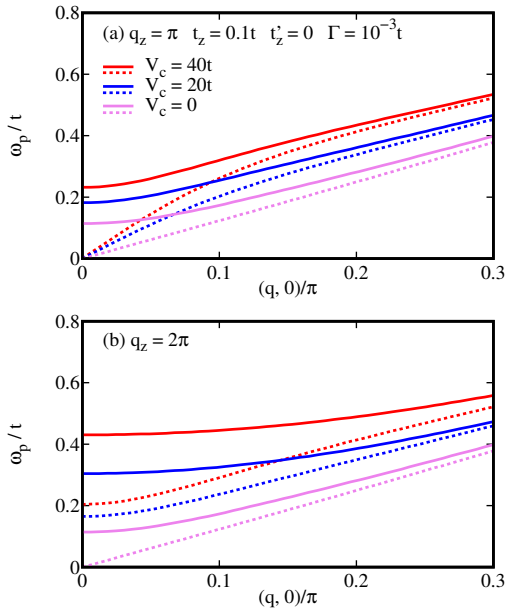

FIG. 12. Dispersive modes along the (0,0)-(0.3π, 0) direction for a sequence of values of V_c. We here employed a smaller broadening $\Gamma = 10^{-3}t$ to trace the dispersion precisely.

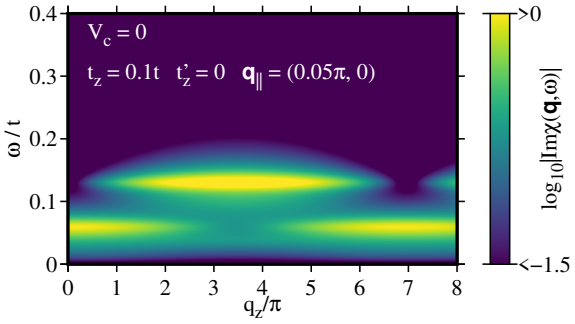

FIG. 13. q_z dependence of spectral weight for $V_c = 0$. While the zero-sound mode is well defined at $q_z = 0$, it evolves smoothly into a lower-energy branch at $q_z \neq 0$. The higher-energy mode is absent at $q_z = 0$, but is realized at a finite q_z.

interestingly, the spectral intensity still exhibits a strong q_z dependence due to the kinetic hopping term along the z direction. Therefore, depending on the value of q_z, the modes may be detected as only one branch, although in principle two branches exist.

IV. DISCUSSIONS

Despite the fundamental difference between our large-N theoretical framework and the RPA [39], we have found that our results for charge dynamics are strikingly similar in many respects, with a few notable differences.

We have used a parameter set closely matching that of Ref. [39], with the exception of the Coulomb potential V_c and the anisotropic parameter α, and temperature. A key difference lies in our use of a significantly smaller value of V_c (in units of t). This disparity reflects the strong correlation effects inherent in the t-J model, which lead to a notable band narrowing effect. This strong correlation is a predominant factor, enabling the plasmon modes to exist across a wide range of momentum space as shown in Fig. 2(a). This sharply contrasts with the RPA results [Fig. 2(b)], where plasmon modes are typically confined to the vicinity of $\mathbf{q}_{\parallel} = (0, 0)$ and becomes heavily damped into the particle-hole continuum as they move further away.

So far there is only one experimental RIXS report [38] in bilayer cuprates where a single q_y-scan was presented. Similar to weak-coupling calculations [39, 40], the present theory—a more adequate theory for cuprates—also suggests that the observed mode is the ω_- mode as shown in Fig. 14. Because of a finite $t_z^{'}$, the ω_- mode will be gapped at $\mathbf{q}_{\parallel} = (0, 0)$. To

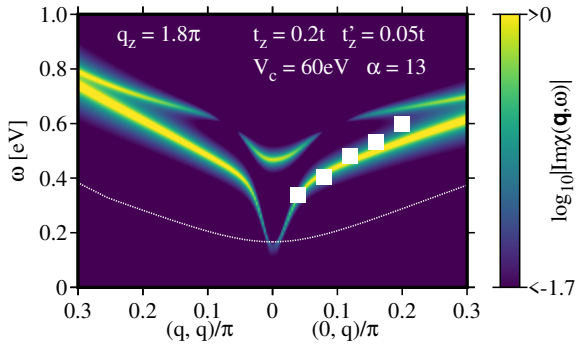

FIG. 14. Comparison with the plasmon energy (solid squares) reported in Y-based cuprate superconductors in Ref. [38]. The experimental data are superimposed on the intensity map of $\log_{10} |\mathrm{Im}\chi(\mathbf{q}, \omega)|$ computed at $q_z = 1.8\pi$ by using $t_z = 0.2t$, $t_z^{'} = 0.05t$, $V_c = 60$ eV, and $\alpha = 13$ (corresponding to $\epsilon_{\parallel} = 1.68\epsilon_0$ and $\epsilon_{\perp} = 1.16\epsilon_0$), keeping the other parameters unchanged; $t/2$ is assumed to be 400 meV. The white dotted curve denotes the upper boundary of the particle-hole continuum.

reinforce this conclusion, we call for more comprehensive data such as q_x-, q_y-, and q_z-scans.

In the bilayer t-J model two collective modes (zero-sound-wavelike modes) remain due to electron correlations. In Appendix B we investigate whether these modes alone could account for the experimental dispersion. Our analysis indicates that this scenario is less consistent with the data, especially regarding the slope of the measured dispersion, and that the plasmon interpretation offers a more coherent description of the observed features.

V. CONCLUSIONS

In this work, we have constructed a strong-coupling theory of bilayer plasmons by employing a large-N formalism for the t-J-V model. Our computational approach of charge excitation spectra was conducted in a matter that allows for a direct comparison with a recent RPA study [39]. Despite the fundamental differences in the theoretical framework, we have found a striking similarity in the plasmon dispersion and intensity maps. This agreement, however, is not without crucial distinctions. In our theory, the strong correlation effects inherent in the t-J model lead to a significant band narrowing, which in turn allows plasmon modes to remain well-defined across the entire Brillouin zone. This stands in sharp contrast to weak-coupling RPA calculations, where plasmons are typically heavily damped away from the zone center.

A unique contribution of our model is the insight gained by systematically varying the Coulomb interaction V_c. We have shown that as V_c is decreased, the plasmon modes change into two distinct modes. When $q_z = 2n\pi$ ($n \neq 0$), one of these modes remains gapped while the other becomes a gapless mode. When $q_z = 0$, only the gapless mode—zero-sound mode—is present. We have also found that while the spectral intensity of these modes shows a strong dependence on q_z, the mode energy itself is remarkably independent of q_z.

The ability of our strong-coupling theory to reproduce plasmon modes provides a comprehensive framework for interpreting experimental data. Our results may offer an explanation for the RIXS data recently obtained in Y-based cuprate superconductors. The ultimate test of the present strong-coupling theory will be the acquisition of more comprehensive RIXS data in bilayer cuprates. If our model provides a coherent explanation for these future results, it would offer compelling evidence that a strong-coupling approach is necessary for describing charge dynamics in these correlated systems.

ACKNOWLEDGMENTS

The authors thank M. Hepting and B. Keimer for valuable discussions about their data, and L. Benfatto, F. Gonzalez, W. Metzner, and I. Pomponio for illuminating discussions. H.Y. was supported by World Premier International Research Center Initiative (WPI), MEXT, Japan. M.B. and A.G. are indebted to warm hospitality of Max-Planck-Institute for Solid State Research. M.B. also thanks MANA Short-Term Invitation Program and warm hospitality in NIMS. A part of the results presented in this work was obtained by using the facilities of the CCT-Rosario Computational Center, member of the High Performance Computing National System (SNCAD, MincyT- Argentina).

Appendix A: Large-N formalism of the bilayer t-J-V model

A major challenge in handling the t-J model arises from the non-double-occupancy constraint. To rigorously enforce the local constraint [Eq. (2)], we express the Hamiltonian in terms of the Hubbard operators $\hat{X}$[57]. The constraint is then implicitly described by the algebra of these operators: $\tilde{c}^{\dagger}_{i\sigma,\alpha} = \hat{X}^{\sigma 0}_{i\alpha}$, $\tilde{c}_{i\sigma,\alpha} = \hat{X}^{0\sigma}_{i\alpha}$, $S^{+}_{i,\alpha} = \hat{X}^{\uparrow\downarrow}_{i\alpha}$, $S^{-}_{i,\alpha} = \hat{X}^{\downarrow\uparrow}_{i\alpha}$, $n_{i,\alpha} = \hat{X}^{\uparrow\uparrow}_{i\alpha} + \hat{X}^{\downarrow\downarrow}_{i\alpha}$, and $\hat{X}^{00}_{i\alpha}$ describes the number of doped holes. The z component of the spin operator is $S^{z}_{i,\alpha} = \frac{1}{2}(\hat{X}^{\uparrow\uparrow}_{i\alpha} - \hat{X}^{\downarrow\downarrow}_{i\alpha})$. The operators $\hat{X}^{\sigma 0}_{i\alpha}$ and $\hat{X}^{0\sigma}_{i\alpha}$ are called fermionlike, whereas the operators $\hat{X}^{\sigma\sigma'}_{i\alpha}$ and $\hat{X}^{00}_{i\alpha}$ are bosonlike.

The Hamiltonian in Eq. (1) can be expressed in terms of the Hubbard operators as:

$$H = -\sum_{i,j,\sigma,\alpha,\beta} t^{\alpha\beta}_{ij} X^{\sigma 0}_{i\alpha} X^{0\sigma}_{j\beta} - \mu \sum_{i,\sigma,\alpha} X^{\sigma\sigma}_{i\alpha} + \frac{J}{2} \sum_{\langle i,j\rangle,\sigma,\sigma',\alpha} \left(X^{\sigma\sigma'}_{i\alpha} X^{\sigma'\sigma}_{j\alpha} - X^{\sigma\sigma}_{i\alpha} X^{\sigma'\sigma'}_{j\alpha} \right) + \frac{J_{\perp}}{4} \sum_{i,\sigma,\sigma',\alpha\neq\beta} \left(X^{\sigma\sigma'}_{i\alpha} X^{\sigma'\sigma}_{i\beta} - X^{\sigma\sigma}_{i\alpha} X^{\sigma'\sigma'}_{i\beta} \right) + \frac{1}{2} \sum_{i\neq j,\sigma,\sigma',\alpha,\beta} V^{\alpha\beta}_{ij} X^{\sigma\sigma}_{i\alpha} X^{\sigma'\sigma'}_{j\beta} \ . \tag{A1}$$

The formalism starts with the construction of a first-order classical Lagrangian using the Faddeev-Jackiw and Dirac methods [58–60]. In this representation, the fermionlike (bosonlike) Hubbard operators are associated with Grassmann (usual bosonic) variables. Next, a large-N expansion is applied to the spin projection, extending it from $\sigma = \uparrow, \downarrow$ to $p = 1, ..., N$ and rescaling the amplitude as $t^{\alpha\beta}_{ij}/N$, J/N, $J_{\perp}/N$, and $V^{\alpha\beta}_{ij}/N$ to ensure a finite theory in the limit of $N \to \infty$. Using the condition

$$X^{pp'}_{i\alpha} = \frac{X^{p0}_{i\alpha} X^{0p'}_{i\alpha}}{X^{00}_{i\alpha}} \tag{A2}$$

for J- and $J_\perp$-terms, we write the fermionlike fields as

$$f^\dagger_{ip,\alpha} = \frac{1}{\sqrt{N\delta/2}} X^{p0}_{i\alpha} \,, \tag{A3}$$

$$f_{ip,\alpha} = \frac{1}{\sqrt{N\delta/2}} X^{0p}_{i\alpha} \,, \tag{A4}$$

where δ is the hole doping away from half-filling. $X^{\sigma\sigma}_{i\alpha}$ in J-, $J_\perp$- and $V^{\alpha\beta}_{ij}$-terms are, on the other hand, treated by utilizing the local constraint $X^{00}_{i\alpha} + \sum_p X^{pp}_{i\alpha} = N/2$ and this constraint is imposed by introducing the Lagrange multiplier $\lambda_{i\alpha}$.

The fields $X^{00}_{i\alpha}$ and $\lambda_{i\alpha}$ are expressed in terms of their static mean-field components and dynamic fluctuations:

$$X^{00}_{i\alpha} = N\frac{\delta}{2}\left(1 + \delta R_{i\alpha}\right), \tag{A5}$$

$$\lambda_{i\alpha} = \lambda_0 + \delta\lambda_{i\alpha} \,, \tag{A6}$$

where $\delta R_{i\alpha}$ denotes the fluctuation of the hole density at site i in layer α; $\delta\lambda_{i\alpha}$ is the fluctuation of the Lagrange multiplier to enforce the constraint against double occupancy.

The resulting effective Lagrangian includes two distinct four-fermion interaction terms, one from the in-plane exchange interaction J, and the other from the out-of-plane interaction $J_\perp$. To decouple these terms, we introduce Hubbard-Stratonovich fields $\Delta_{ij,\alpha}$ and Δ'_i:

$$\Delta_{ij,\alpha} = \frac{J}{2}\sum_p \frac{f^\dagger_{jp,\alpha} f_{ip,\alpha}}{\sqrt{(1+\delta R_{i\alpha})(1+\delta R_{j\alpha})}} \,, \tag{A7}$$

$$\Delta'_i = \frac{J_\perp}{4}\sum_p \frac{f^\dagger_{ip,1} f_{ip,2}}{\sqrt{(1+\delta R_{i1})(1+\delta R_{i2})}} \,. \tag{A8}$$

The fields $\Delta_{ij,\alpha}$ and Δ'_i describe bond-charge fluctuations in the intralayer and intrabilayer, respectively. Since i and j are nearest-neighbor sites on the square lattice, we may write $\Delta_{ij,\alpha} = \Delta^\eta_{i\alpha}$ where $\eta = x$ or y. We parametrize those fields as:

$$\Delta^\eta_{i\alpha} = \chi\left(1 + r^\eta_{i\alpha} + \mathrm{i}A^\eta_{i\alpha}\right) \,, \tag{A9}$$

$$\Delta'_i = \chi'\left(1 + r_{\perp,i} + \mathrm{i}A_{\perp,i}\right) \,, \tag{A10}$$

where $r^\eta_{i\alpha}$ and $A^\eta_{i\alpha}$ ($r_{\perp,i}$ and $A_{\perp,i}$) represent the real and imaginary parts of the in-plane (out-of-plane) bond-field fluctuations, respectively, and χ (χ') is the corresponding static mean-field value.

Finally, the terms involving $1/\sqrt{1+\delta R_{i\alpha}}$ are expanded perturbatively in powers of $\delta R_{i\alpha}$. This expansion systematically organizes the interactions in powers of $1/N$, thus controlling the hierarchy of contributions in the large-N formalism. The effective theory of Eq. (1) is then described in terms of fermions, bosons, and their interactions.

In the large-N formalism for bilayer systems, we introduce a 14-component bosonic field as a basis:

$$\delta X^a = (\delta R_1,\ \delta\lambda_1,\ \delta R_2,\ \delta\lambda_2,\ r_1^x,\ r_1^y,\ A_1^x,\ A_1^y,\ r_2^x,\ r_2^y,\ A_2^x,\ A_2^y,\ r_\perp,\ A_\perp)\,, \tag{A11}$$

where the site index is omitted for clarity.

Following Refs. [52, 61, 62], the Feynman rules applied to the effective theory give a 14×14 bare bosonic propagator $D^{(0)}_{ab}(\mathbf{q}, \mathrm{i}\omega_n)$ that is $O(1/N)$:

$$\left[D^{(0)}_{ab}(\mathbf{q}, \mathrm{i}\omega_n)\right]^{-1} = N \begin{pmatrix} D_A^{(0)} & D_B^{(0)} & 0 & 0 & 0 \\ D_B^{(0)*} & D_A^{(0)} & 0 & 0 & 0 \\ 0 & 0 & D_C^{(0)} & 0 & 0 \\ 0 & 0 & 0 & D_C^{(0)} & 0 \\ 0 & 0 & 0 & 0 & D_D^{(0)} \end{pmatrix}, \tag{A12}$$

where ω_n is a bosonic Matsubara frequency and the matrices $D^{(0)}_{A\text{-}D}$ are:

$$D_A^{(0)} = \begin{pmatrix} \frac{\delta^2}{2}\left[\frac{V(\mathbf{q})}{2} - J(\mathbf{q})\right] & \frac{\delta}{2} \\ \frac{\delta}{2} & 0 \end{pmatrix}, \tag{A13}$$

$$D_B^{(0)} = \begin{pmatrix} \frac{\delta^2}{2}\left[\frac{V'(\mathbf{q})}{2} - J'(\mathbf{q})\right] & 0 \\ 0 & 0 \end{pmatrix}, \tag{A14}$$

$$D_C^{(0)} = \begin{pmatrix} \frac{4\chi^2}{J} & 0 & 0 & 0 \\ 0 & \frac{4\chi^2}{J} & 0 & 0 \\ 0 & 0 & \frac{4\chi^2}{J} & 0 \\ 0 & 0 & 0 & \frac{4\chi^2}{J} \end{pmatrix}, \tag{A15}$$

$$D_D^{(0)} = \begin{pmatrix} \frac{4\chi'^2}{J_\perp} & 0 \\ 0 & \frac{4\chi'^2}{J_\perp} \end{pmatrix}. \tag{A16}$$

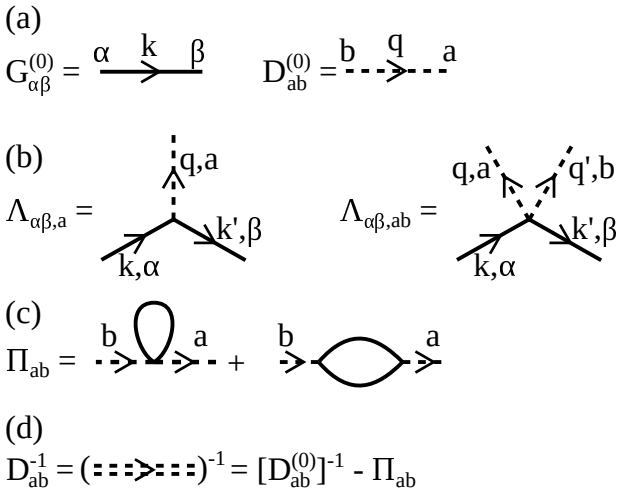

FIG. 15. (a) Bare fermionic $G^{(0)}_{\alpha\beta}$ and bosonic $D^{(0)}_{ab}$ propagators, solid and dashed lines, respectively. (b) $\Lambda_{\alpha\beta,a}$ and $\Lambda_{\alpha\beta,ab}$ are the three- and four-legs vertices, respectively. (c) Π_{ab} is the bosonic self-energy. (d) Double dashed line is the dressed bosonic propagator D_{ab}.

The large-N formalism yields the bare bosonic propagator as a 14×14 matrix [see Eq. (A12)]. However, because we focus on on-site charge excitations, including plasmons [63], we restrict our analysis to the corresponding 4×4 submatrix of the bare bosonic propagator given by

$$\left[D^{(0)}_{ab}(\mathbf{q}, \mathrm{i}\omega_n)\right]^{-1} = N \begin{pmatrix} \frac{\delta^2}{2}\left[\frac{V(\mathbf{q})}{2} - J(\mathbf{q})\right] & \frac{\delta}{2} & \frac{\delta^2}{2}\left[\frac{V'(\mathbf{q})}{2} - J'(\mathbf{q})\right] & 0 \\ \frac{\delta}{2} & 0 & 0 & 0 \\ \frac{\delta^2}{2}\left[\frac{V'^*(\mathbf{q})}{2} - J'^*(\mathbf{q})\right] & 0 & \frac{\delta^2}{2}\left[\frac{V(\mathbf{q})}{2} - J(\mathbf{q})\right] & \frac{\delta}{2} \\ 0 & 0 & \frac{\delta}{2} & 0 \end{pmatrix}, \tag{A17}$$

where the matrix elements are limited to $a, b = \delta R_a, \delta\lambda_a$.

Interactions between bosons and fermions are governed by three- and four-leg vertices. The three-leg vertex $\Lambda_{\alpha\beta,a}$ represents the interaction of a fermion from layer α that ends at layer β after interacting with a boson δX^a. We can write this vertex as

$$\Lambda_{\alpha\beta,a}(k, k', q) = \tilde{\Lambda}_{\alpha\beta,a}(k, k', q)\mathrm{e}^{\mathrm{i}(-k_z d_\alpha + k'_z d_\beta + q_z d_a)}\delta(k - k' - q) \tag{A18}$$

where $k \equiv \mathbf{k}, \mathrm{i}\nu_n$, $q \equiv \mathbf{q}, \mathrm{i}\omega_n$ and d_a is equal to d_1 or d_2 depending on the plane of the boson δX^a, with $d_1 = 0$ and $d_2 = d/c$. After executing $\delta(k - k' - q)$, the nonzero components of $\tilde{\Lambda}_{\alpha\beta,a}(k, k', q)$ in the charge sector become

$$\tilde{\Lambda}_{\alpha\alpha,a}(k,q) = -\left[\mathrm{i}\nu_n - \frac{\mathrm{i}\omega_n}{2} + \mu + 2\chi \sum_{\eta=x,y} \cos\left(k_\eta - \frac{q_\eta}{2}\right) \cos\frac{q_\eta}{2},\ 1\right] \tag{A19}$$

for each component $a = \delta R_\alpha,\ \delta\lambda_\alpha$. For $\alpha \neq \beta$

$$\tilde{\Lambda}_{\alpha\beta,a}(k,q) = -\left(\frac{\chi'}{2}, \frac{\chi'}{2}\right) \tag{A20}$$

for each component $a = \delta R_1,\ \delta R_2$.

The four-leg vertex $\Lambda_{\alpha\beta,ab}$ represents a fermion from layer α that ends in layer β after interacting with the bosons δX^a and δX^b. We write this vertex as

$$\Lambda_{\alpha\beta,ab}(k,k',q,q') = \tilde{\Lambda}_{\alpha\beta,ab}(k,k',q,q')\mathrm{e}^{\mathrm{i}(-k_z d_\alpha + k'_z d_\beta + q_z d_a + q'_z d_b)}\delta(k - k' - q - q')\ , \tag{A21}$$

where, after executing $\delta(k - k' - q - q')$, the nonzero components of $\tilde{\Lambda}_{\alpha\beta,ab}(k,k',q,q')$ in the charge sector become

$$\tilde{\Lambda}_{\alpha\alpha,ab}(k,q,q') = \begin{bmatrix} F_{k,q,q'} & 1/2 \\ 1/2 & 0 \end{bmatrix} \tag{A22}$$

for each component $a, b = \delta R_\alpha,\ \delta\lambda_\alpha$, where

$$\begin{aligned} F_{k,q,q'} = \mathrm{i}\nu_n - \frac{\mathrm{i}\omega_n + \mathrm{i}\omega'_n}{2} + \mu + \chi \sum_{\eta=x,y} \cos\left(k_\eta - \frac{q_\eta + q'_\eta}{2}\right) \\ \times \left[\cos\left(\frac{q_\eta + q'_\eta}{2}\right) + \cos\frac{q_\eta}{2}\cos\frac{q'_\eta}{2}\right]\ . \end{aligned} \tag{A23}$$

For $\alpha \neq \beta$

$$\tilde{\Lambda}_{\alpha\beta,ab} = \frac{\chi'}{8}\begin{bmatrix} 3 & 1 \\ 1 & 3 \end{bmatrix} \tag{A24}$$

for each component $a, b = \delta R_1,\ \delta R_2$. Note that the vertices are $O(1)$.

Using the propagators [Eq. (3) and Fig. 15(a)] and vertices [Fig. 15(b)] the bosonic self-energy $\Pi_{ab}(\mathbf{q}, \mathrm{i}\omega_n)$ [Fig. 15(c)] is computed, considering both Hartree and bubble diagrams. The Dyson equation [Fig. 15(d)] yields the dressed bosonic propagator $D_{ab}(\mathbf{q}, \mathrm{i}\omega_n)$ as

$$D^{-1}_{ab}(\mathbf{q}, \mathrm{i}\omega_n) = \left[D^{(0)}_{ab}(\mathbf{q}, \mathrm{i}\omega_n)\right]^{-1} - \Pi_{ab}(\mathbf{q}, \mathrm{i}\omega_n)\,. \tag{A25}$$

Focusing on the 4×4 charge sector of the self-energy, the analytical expressions of each component are:

$$\Pi_{11}(\mathbf{q}, \mathrm{i}\omega_n) = -\frac{N}{16N_s} \sum_{\alpha,\beta=1}^{2} \sum_{\mathbf{k}} \left[n_F\left(\varepsilon^{\alpha}_{\mathbf{k}-\mathbf{q}}\right) - n_F\left(\varepsilon^{\beta}_{\mathbf{k}}\right) \right] \left(\tilde{\varepsilon}^{\beta}_{\mathbf{k}} - \tilde{\varepsilon}^{\alpha}_{\mathbf{k}-\mathbf{q}} \right) + \left(\tilde{\varepsilon}^{\beta}_{\mathbf{k}} + \tilde{\varepsilon}^{\alpha}_{\mathbf{k}-\mathbf{q}} \right)^2 g^{\alpha\beta} \ , \tag{A26}$$

$$\Pi_{12}(\mathbf{q}, \mathrm{i}\omega_n) = -\frac{N}{8N_s} \sum_{\alpha,\beta=1}^{2} \sum_{\mathbf{k}} \left(\tilde{\varepsilon}^{\beta}_{\mathbf{k}} + \tilde{\varepsilon}^{\alpha}_{\mathbf{k}-\mathbf{q}} \right) g^{\alpha\beta} \ , \tag{A27}$$

$$\begin{aligned}\Pi_{13}(\mathbf{q}, \mathrm{i}\omega_n) = &- \mathrm{e}^{-\mathrm{i}q_z \frac{d}{c}} \frac{N}{16N_s} \sum_{\alpha,\beta=1}^{2} (-1)^{\alpha+\beta} \sum_{\mathbf{k}} \frac{\varepsilon^{\perp *}_{\mathbf{k}-\mathbf{q}} \varepsilon^{\perp}_{\mathbf{k}}}{|\varepsilon^{\perp}_{\mathbf{k}-\mathbf{q}}||\varepsilon^{\perp}_{\mathbf{k}}|} \left\{ \left[n_F\left(\varepsilon^{\alpha}_{\mathbf{k}-\mathbf{q}}\right) - n_F\left(\varepsilon^{\beta}_{\mathbf{k}}\right) \right] \left(\tilde{\varepsilon}^{\beta}_{\mathbf{k}} - \tilde{\varepsilon}^{\alpha}_{\mathbf{k}-\mathbf{q}} \right) \right. \\ &\left. + \left(\tilde{\varepsilon}^{\beta}_{\mathbf{k}} + \tilde{\varepsilon}^{\alpha}_{\mathbf{k}-\mathbf{q}} \right)^2 g^{\alpha\beta} \right\} \ ,\end{aligned} \tag{A28}$$

$$\begin{aligned}\Pi_{31}(\mathbf{q}, \mathrm{i}\omega_n) = &- \mathrm{e}^{\mathrm{i}q_z \frac{d}{c}} \frac{N}{16N_s} \sum_{\alpha,\beta=1}^{2} (-1)^{\alpha+\beta} \sum_{\mathbf{k}} \frac{\varepsilon^{\perp}_{\mathbf{k}-\mathbf{q}} \varepsilon^{\perp *}_{\mathbf{k}}}{|\varepsilon^{\perp}_{\mathbf{k}-\mathbf{q}}||\varepsilon^{\perp}_{\mathbf{k}}|} \left\{ \left[n_F\left(\varepsilon^{\alpha}_{\mathbf{k}-\mathbf{q}}\right) - n_F\left(\varepsilon^{\beta}_{\mathbf{k}}\right) \right] \left(\tilde{\varepsilon}^{\beta}_{\mathbf{k}} - \tilde{\varepsilon}^{\alpha}_{\mathbf{k}-\mathbf{q}} \right) \right. \\ &\left. + \left(\tilde{\varepsilon}^{\beta}_{\mathbf{k}} + \tilde{\varepsilon}^{\alpha}_{\mathbf{k}-\mathbf{q}} \right)^2 g^{\alpha\beta} \right\} \ ,\end{aligned} \tag{A29}$$

$$\Pi_{14}(\mathbf{q}, \mathrm{i}\omega_n) = -\mathrm{e}^{-\mathrm{i}q_z \frac{d}{c}} \frac{N}{8N_s} \sum_{\alpha,\beta=1}^{2} (-1)^{\alpha+\beta} \sum_{\mathbf{k}} \frac{\varepsilon^{\perp *}_{\mathbf{k}-\mathbf{q}} \varepsilon^{\perp}_{\mathbf{k}}}{|\varepsilon^{\perp}_{\mathbf{k}-\mathbf{q}}||\varepsilon^{\perp}_{\mathbf{k}}|} \left(\tilde{\varepsilon}^{\beta}_{\mathbf{k}} + \tilde{\varepsilon}^{\alpha}_{\mathbf{k}-\mathbf{q}} \right) g^{\alpha\beta} \tag{A30}$$

$$\Pi_{41}(\mathbf{q}, \mathrm{i}\omega_n) = -\mathrm{e}^{\mathrm{i}q_z \frac{d}{c}} \frac{N}{8N_s} \sum_{\alpha,\beta=1}^{2} (-1)^{\alpha+\beta} \sum_{\mathbf{k}} \frac{\varepsilon^{\perp}_{\mathbf{k}-\mathbf{q}} \varepsilon^{\perp *}_{\mathbf{k}}}{|\varepsilon^{\perp}_{\mathbf{k}-\mathbf{q}}||\varepsilon^{\perp}_{\mathbf{k}}|} \left(\tilde{\varepsilon}^{\beta}_{\mathbf{k}} + \tilde{\varepsilon}^{\alpha}_{\mathbf{k}-\mathbf{q}} \right) g^{\alpha\beta} \tag{A31}$$

$$\Pi_{22}(\mathbf{q}, \mathrm{i}\omega_n) = -\frac{N}{4N_s} \sum_{\alpha,\beta=1}^{2} \sum_{\mathbf{k}} g^{\alpha\beta} \tag{A32}$$

$$\Pi_{24}(\mathbf{q}, \mathrm{i}\omega_n) = -\mathrm{e}^{-\mathrm{i}q_z \frac{d}{c}} \frac{N}{4N_s} \sum_{\alpha,\beta=1}^{2} (-1)^{\alpha+\beta} \sum_{\mathbf{k}} \frac{\varepsilon^{\perp *}_{\mathbf{k}-\mathbf{q}} \varepsilon^{\perp}_{\mathbf{k}}}{|\varepsilon^{\perp}_{\mathbf{k}-\mathbf{q}}||\varepsilon^{\perp}_{\mathbf{k}}|} g^{\alpha\beta} \ , \tag{A33}$$

$$\Pi_{42}(\mathbf{q}, \mathrm{i}\omega_n) = -\mathrm{e}^{\mathrm{i}q_z \frac{d}{c}} \frac{N}{4N_s} \sum_{\alpha,\beta=1}^{2} (-1)^{\alpha+\beta} \sum_{\mathbf{k}} \frac{\varepsilon^{\perp}_{\mathbf{k}-\mathbf{q}} \varepsilon^{\perp *}_{\mathbf{k}}}{|\varepsilon^{\perp}_{\mathbf{k}-\mathbf{q}}||\varepsilon^{\perp}_{\mathbf{k}}|} g^{\alpha\beta} \ , \tag{A34}$$

$$\Pi_{21}(\mathbf{q}, \mathrm{i}\omega_n) = \Pi_{34}(\mathbf{q}, \mathrm{i}\omega_n) = \Pi_{43}(\mathbf{q}, \mathrm{i}\omega_n) = \Pi_{12}(\mathbf{q}, \mathrm{i}\omega_n) \ , \tag{A35}$$

$$\Pi_{23}(\mathbf{q}, \mathrm{i}\omega_n) = \Pi_{14}(\mathbf{q}, \mathrm{i}\omega_n) \ , \tag{A36}$$

$$\Pi_{32}(\mathbf{q}, \mathrm{i}\omega_n) = \Pi_{41}(\mathbf{q}, \mathrm{i}\omega_n) \ , \tag{A37}$$

$$\Pi_{33}(\mathbf{q}, \mathrm{i}\omega_n) = \Pi_{11}(\mathbf{q}, \mathrm{i}\omega_n) \ , \tag{A38}$$

$$\Pi_{44}(\mathbf{q}, \mathrm{i}\omega_n) = \Pi_{22}(\mathbf{q}, \mathrm{i}\omega_n) \ , \tag{A39}$$

where $\tilde{\varepsilon}^{\alpha}_{\mathbf{k}}$ is equal to $\varepsilon^{\alpha}_{\mathbf{k}}$ with $\mu = \chi = \chi' = 0$, and

$$g^{\alpha\beta} = \frac{n_F\left(\varepsilon^{\alpha}_{\mathbf{k}-\mathbf{q}}\right) - n_F\left(\varepsilon^{\beta}_{\mathbf{k}}\right)}{\mathrm{i}\omega_n + \varepsilon^{\alpha}_{\mathbf{k}-\mathbf{q}} - \varepsilon^{\beta}_{\mathbf{k}}} \,. \tag{A40}$$

Appendix B: Analysis of experimental data with $V_c = 0$

In Sec. III C we showed that two collective modes persist even when the long-range Coulomb interaction is switched off ($V_c = 0$). In this section we examine whether the experimental dispersion in Fig. 14 could be interpreted within this scenario.

A first qualitative consideration already points to a limitation: the lower-energy zero-sound-wavelike mode necessarily decreases linearly to zero as $\mathbf{q}_{\parallel} \to (0, 0)$, whereas the experimental data show no indication of such behavior. This implies that, if a zero-sound-based interpretation were to be considered, the relevant branch would need to be the higher-energy mode.

Figure 16(a) shows the intensity map for $V_c = 0$ using the same band parameters that successfully describe the plasmon dispersion in Fig. 14. The resulting zero-sound-wavelike branches lie at substantially lower energies than the experimental data, indicating that these parameters cannot account for the measured spectrum. To counteract this effect, we

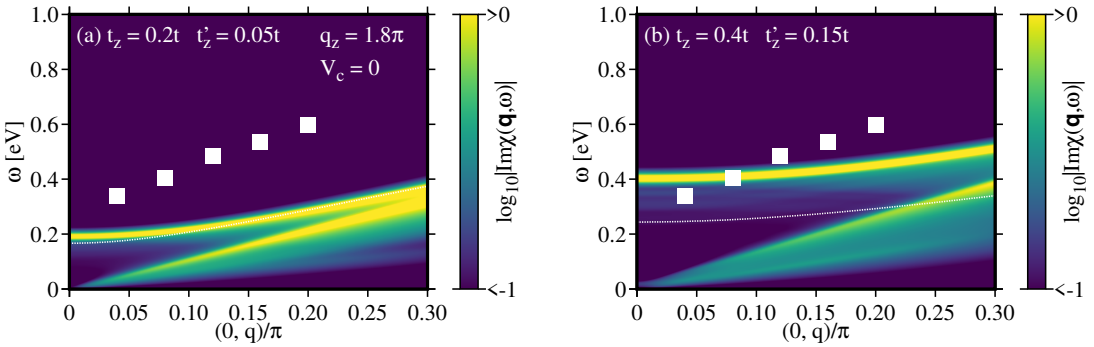

FIG. 16. Comparison with the plasmon energy (solid squares) reported in Y-based cuprate superconductors in Ref. [38]. The experimental data are superimposed on the intensity map of $\log_{10}|\mathrm{Im}\chi(\mathbf{q},\omega)|$ computed at $q_z = 1.8\pi$ with $V_c = 0$ by using (a) $t_z = 0.2t$, $t_z^{'} = 0.05t$ (same as in Fig. 14), and (b) $t_z = 0.4t$, $t_z^{'} = 0.15t$, while keeping the other parameters unchanged; $t/2$ is assumed to be 400 meV. The white dotted curve denotes the upper boundary of the particle-hole continuum.

consider larger values of t_z and $t_z^{'}$ and display the corresponding results in Fig. 16(b). While the overall energy scale then becomes comparable to the measured one, the slope of the computed dispersion remains inconsistent with the observed trend. Moreover, the required values of t_z and $t_z^{'}$ appear too large for bilayer cuprates, suggesting that a description based solely on zero-sound-wavelike modes is unlikely.

These analyses lead us to conclude that the experimental features cannot be satisfactorily described by the collective modes of the pure bilayer t-J model. Instead, their dispersion and spectral characteristics are more naturally and consistently interpreted in terms of plasmons.

---

[1] B. Keimer, S. A. Kivelson, M. R. Norman, S. Uchida, and J. Zaanen, "From quantum matter to high-temperature superconductivity in copper oxides," Nature **518**, 179–186 (2015).

[2] P. W. Anderson, "The resonating valence bond state in La_2CuO_4 and superconductivity," Science **235**, 1196–1198 (1987).

[3] Luuk J. P. Ament, Michel van Veenendaal, Thomas P. Devereaux, John P. Hill, and Jeroen van den Brink, "Resonant inelastic x-ray scattering studies of elementary excitations," Rev. Mod. Phys. **83**, 705–767 (2011).

[4] Frank M. F. de Groot, Maurits W. Haverkort, Hebatalla Elnaggar, Amélie Juhin, Ke-Jin Zhou, and Pieter Glatzel, "Resonant inelastic x-ray scattering," Nature Reviews Methods Primers **4**, 45 (2024).

[5] G. Ghiringhelli, M. Le Tacon, M. Minola, S. Blanco-Canosa, C. Mazzoli, N. B. Brookes, G. M. De Luca, A. Frano, D. G. Hawthorn, F. He, T. Loew, M. Moretti Sala, D. C. Peets, M. Salluzzo, E. Schierle, R. Sutarto, G. A. Sawatzky, E. Weschke, B. Keimer, and L. Braicovich, "Long-Range Incommensurate Charge Fluctuations in (Y,Nd)$Ba_2Cu_3O_{6+x}$," Science **337**, 821–825 (2012).

[6] J. Chang, E. Blackburn, A. T. Holmes, N. B. Christensen, J. Larsen, J. Mesot, Ruixing Liang, D. A. Bonn, W. N. Hardy, A. Watenphul, M. v. Zimmermann, E. M. Forgan, and S. M. Hayden, "Direct observation of competition between superconductivity and charge density wave order in $YBa_2Cu_3O_{6.67}$," Nat. Phys. **8**, 871 (2012).

[7] A. J. Achkar, R. Sutarto, X. Mao, F. He, A. Frano, S. Blanco-Canosa, M. Le Tacon, G. Ghiringhelli, L. Braicovich, M. Minola, M. Moretti Sala, C. Mazzoli, Ruixing Liang, D. A. Bonn,

W. N. Hardy, B. Keimer, G. A. Sawatzky, and D. G. Hawthorn, "Distinct Charge Orders in the Planes and Chains of Ortho-III-Ordered $YBa_2Cu_3O_{6+\delta}$ Superconductors Identified by Resonant Elastic X-ray Scattering," Phys. Rev. Lett. **109**, 167001 (2012).

[8] E. Blackburn, J. Chang, M. Hücker, A. T. Holmes, N. B. Christensen, Ruixing Liang, D. A. Bonn, W. N. Hardy, U. Rütt, O. Gutowski, M. v. Zimmermann, E. M. Forgan, and S. M. Hayden, "X-Ray Diffraction Observations of a Charge-Density-Wave Order in Superconducting Ortho-II $YBa_2Cu_3O_{6.54}$ Single Crystals in Zero Magnetic Field," Phys. Rev. Lett. **110**, 137004 (2013).

[9] S. Blanco-Canosa, A. Frano, E. Schierle, J. Porras, T. Loew, M. Minola, M. Bluschke, E. Weschke, B. Keimer, and M. Le Tacon, "Resonant x-ray scattering study of charge-density wave correlations in $YBa_2Cu_3O_{6+x}$," Phys. Rev. B **90**, 054513 (2014).

[10] R. Comin, A. Frano, M. M. Yee, Y. Yoshida, H. Eisaki, E. Schierle, E. Weschke, R. Sutarto, F. He, A. Soumyanarayanan, Yang He, M. Le Tacon, I. S. Elfimov, Jennifer E. Hoffman, G. A. Sawatzky, B. Keimer, and A. Damascelli, "Charge Order Driven by Fermi-Arc Instability in $Bi_2Sr_{2-x}La_xCuO_{6+\delta}$," Science **343**, 390–392 (2014).

[11] W. Tabis, Y. Li, M. Le Tacon, L. Braicovich, A. Kreyssig, M. Minola, G. Dellea, E. Weschke, M. J. Veit, M. Ramazanoglu, A. I. Goldman, T. Schmitt, G. Ghiringhelli, N. Barisic, M. K. Chan, C. J. Dorow, G. Yu, X. Zhao, B. Keimer, and M. Greven, "Charge order and its connection with Fermi-liquid charge transport in a pristine high-T_c cuprate," Nat. Commun. **5**, 5875 (2014).

[12] Eduardo H. da Silva Neto, Pegor Aynajian, Alex Frano, Riccardo Comin, Enrico Schierle, Eugen Weschke, András Gyenis, Jinsheng Wen, John Schneeloch, Zhijun Xu, Shimpei Ono, Genda Gu, Mathieu Le Tacon, and Ali Yazdani, "Ubiquitous interplay between charge ordering and high-temperature superconductivity in cuprates," Science **343**, 393–396 (2014).

[13] M. Hashimoto, G. Ghiringhelli, W.-S. Lee, G. Dellea, A. Amorese, C. Mazzoli, K. Kummer, N. B. Brookes, B. Moritz, Y. Yoshida, H. Eisaki, Z. Hussain, T. P. Devereaux, Z.-X. Shen, and L. Braicovich, "Direct observation of bulk charge modulations in optimally doped $Bi_{1.5}Pb_{0.6}Sr_{1.54}CaCu_2O_{8+\delta}$," Phys. Rev. B **89**, 220511 (2014).

[14] Y. Y. Peng, M. Salluzzo, X. Sun, A. Ponti, D. Betto, A. M. Ferretti, F. Fumagalli, K. Kummer, M. Le Tacon, X. J. Zhou, N. B. Brookes, L. Braicovich, and G. Ghiringhelli, "Direct observation of charge order in underdoped and optimally doped $Bi_2(Sr,La)_2CuO_{6+\delta}$ by resonant

inelastic x-ray scattering," Phys. Rev. B **94**, 184511 (2016).

[15] L. Chaix, G. Ghiringhelli, Y. Y. Peng, M. Hashimoto, B. Moritz, K. Kummer, N. B. Brookes, Y. He, S. Chen, S. Ishida, Y. Yoshida, H. Eisaki, M. Salluzzo, L. Braicovich, Z. X. Shen, T. P. Devereaux, and W. S. Lee, "Dispersive charge density wave excitations in $Bi_2Sr_2CaCu_2O_{8+\delta}$," Nat. Phys. **13**, 952 (2017).

[16] R. Arpaia, S. Caprara, R. Fumagalli, G. De Vecchi, Y. Y. Peng, E. Andersson, D. Betto, G. M. De Luca, N. B. Brookes, F. Lombardi, M. Salluzzo, L. Braicovich, C. Di Castro, M. Grilli, and G. Ghiringhelli, "Dynamical charge density fluctuations pervading the phase diagram of a Cu-based high-T_c superconductor," Science **365**, 906–910 (2019).

[17] B. Yu, W. Tabis, I. Bialo, F. Yakhou, N. B. Brookes, Z. Anderson, Y. Tang, G. Yu, and M. Greven, "Unusual dynamic charge correlations in simple-tetragonal $HgBa_2CuO_{4+\delta}$," Phys. Rev. X **10**, 021059 (2020).

[18] W. S. Lee, Ke-Jin Zhou, M. Hepting, J. Li, A. Nag, A. C. Walters, M. Garcia-Fernandez, H. C. Robarts, M. Hashimoto, H. Lu, B. Nosarzewski, D. Song, H. Eisaki, Z. X. Shen, B. Moritz, J. Zaanen, and T. P. Devereaux, "Spectroscopic fingerprint of charge order melting driven by quantum fluctuations in a cuprate," Nat. Phys. **17**, 53–57 (2021).

[19] Haiyu Lu, Makoto Hashimoto, Su-Di Chen, Shigeyuki Ishida, Dongjoon Song, Hiroshi Eisaki, Abhishek Nag, Mirian Garcia-Fernandez, Riccardo Arpaia, Giacomo Ghiringhelli, Lucio Braicovich, Jan Zaanen, Brian Moritz, Kurt Kummer, Nicholas B. Brookes, Ke-Jin Zhou, Zhi-Xun Shen, Thomas P. Devereaux, and Wei-Sheng Lee, "Identification of a characteristic doping for charge order phenomena in Bi-2212 cuprates via RIXS," Phys. Rev. B **106**, 155109 (2022).

[20] Riccardo Arpaia, Leonardo Martinelli, Marco Moretti Sala, Sergio Caprara, Abhishek Nag, Nicholas B. Brookes, Pietro Camisa, Qizhi Li, Qiang Gao, Xingjiang Zhou, Mirian Garcia-Fernandez, Ke-Jin Zhou, Enrico Schierle, Thilo Bauch, Ying Ying Peng, Carlo Di Castro, Marco Grilli, Floriana Lombardi, Lucio Braicovich, and Giacomo Ghiringhelli, "Signature of quantum criticality in cuprates by charge density fluctuations," Nat. Commun. **14**, 7198 (2023).

[21] (), the charge order observed in La-based cuprates is often discussed in terms of the spin-charge stripe order [64]. It is an interesting subject to investigate its possible connection to the newly observed charge ordering tendency around $q_x \sim 0.6\pi$ in other hole-doped cuprates.

[22] Eduardo H. da Silva Neto, Riccardo Comin, Feizhou He, Ronny Sutarto, Yeping Jiang, Richard L. Greene, George A. Sawatzky, and Andrea Damascelli, "Charge ordering in the electron-doped superconductor $Nd_{2-x}Ce_xCuO_4$," Science **347**, 282–285 (2015).

[23] Eduardo H. da Silva Neto, Biqiong Yu, Matteo Minola, Ronny Sutarto, Enrico Schierle, Fabio Boschini, Marta Zonno, Martin Bluschke, Joshua Higgins, Yangmu Li, Guichuan Yu, Eugen Weschke, Feizhou He, Mathieu Le Tacon, Richard L. Greene, Martin Greven, George A. Sawatzky, Bernhard Keimer, and Andrea Damascelli, "Doping-dependent charge order correlations in electron-doped cuprates," Science Advances **2**, e1600782 (2016).

[24] E. H. da Silva Neto, M. Minola, B. Yu, W. Tabis, M. Bluschke, D. Unruh, H. Suzuki, Y. Li, G. Yu, D. Betto, K. Kummer, F. Yakhou, N. B. Brookes, M. Le Tacon, M. Greven, B. Keimer, and A. Damascelli, "Coupling between dynamic magnetic and charge-order correlations in the cuprate superconductor $Nd_{2-x}Ce_xCuO_4$," Phys. Rev. B **98**, 161114 (2018).

[25] K. Ishii, K. Tsutsui, Y. Endoh, T. Tohyama, S. Maekawa, M. Hoesch, K. Kuzushita, M. Tsubota, T. Inami, J. Mizuki, Y. Murakami, and K. Yamada, "Momentum Dependence of Charge Excitations in the Electron-Doped Superconductor $Nd_{1.85}Ce_{0.15}CuO_4$: A Resonant Inelastic X-Ray Scattering Study," Phys. Rev. Lett. **94**, 207003 (2005).

[26] K. Ishii, M. Fujita, T. Sasaki, M. Minola, G. Dellea, C. Mazzoli, K. Kummer, G. Ghiringhelli, L. Braicovich, T. Tohyama, K. Tsutsumi, K. Sato, R. Kajimoto, K. Ikeuchi, K. Yamada, M. Yoshida, M. Kurooka, and J. Mizuki, "High-energy spin and charge excitations in electron-doped copper oxide superconductors," Nat. Commun. **5**, 3714 (2014).

[27] W. S. Lee, J. J. Lee, E. A. Nowadnick, S. Gerber, W. Tabis, S. W. Huang, V. N. Strocov, E. M. Motoyama, G. Yu, B. Moritz, H. Y. Huang, R. P. Wang, Y. B. Huang, W. B. Wu, C. T. Chen, D. J. Huang, M. Greven, T. Schmitt, Z. X. Shen, and T. P. Devereaux, "Asymmetry of collective excitations in electron- and hole-doped cuprate superconductors," Nat. Phys. **10**, 883–889 (2014).

[28] Andrés Greco, Hiroyuki Yamase, and Matías Bejas, "Plasmon excitations in layered high-T_c cuprates," Phys. Rev. B **94**, 075139 (2016).

[29] Kenji Ishii, Takami Tohyama, Shun Asano, Kentaro Sato, Masaki Fujita, Shuichi Wakimoto, Kenji Tustsui, Shigetoshi Sota, Jun Miyawaki, Hideharu Niwa, Yoshihisa Harada, Jonathan Pelliciari, Yaobo Huang, Thorsten Schmitt, Yoshiya Yamamoto, and Jun'ichiro Mizuki, "Observation of momentum-dependent charge excitations in hole-doped cuprates using resonant

inelastic x-ray scattering at the oxygen K edge," Phys. Rev. B **96**, 115148 (2017).

[30] G. Dellea, M. Minola, A. Galdi, D. Di Castro, C. Aruta, N. B. Brookes, C. J. Jia, C. Mazzoli, M. Moretti Sala, B. Moritz, P. Orgiani, D. G. Schlom, A. Tebano, G. Balestrino, L. Braicovich, T. P. Devereaux, L. Maritato, and G. Ghiringhelli, "Spin and charge excitations in artificial hole- and electron-doped infinite layer cuprate superconductors," Phys. Rev. B **96**, 115117 (2017).

[31] M. Hepting, L. Chaix, E. W. Huang, R. Fumagalli, Y. Y. Peng, B. Moritz, K. Kummer, N. B. Brookes, W. C. Lee, M. Hashimoto, T. Sarkar, J.-F. He, C. R. Rotundu, Y. S. Lee, R. L. Greene, L. Braicovich, G. Ghiringhelli, Z. X. Shen, T. P. Devereaux, and W. S. Lee, "Three-dimensional collective charge excitations in electron-doped copper oxide superconductors," Nature **563**, 374–378 (2018).

[32] Andrés Greco, Hiroyuki Yamase, and Matías Bejas, "Origin of high-energy charge excitations observed by resonant inelastic x-ray scattering in cuprate superconductors," Commun. Phys. **2**, 3 (2019).

[33] M. Hepting, M. Bejas, A. Nag, H. Yamase, N. Coppola, D. Betto, C. Falter, M. Garcia-Fernandez, S. Agrestini, Ke-Jin Zhou, M. Minola, C. Sacco, L. Maritato, P. Orgiani, H. I. Wei, K. M. Shen, D. G. Schlom, A. Galdi, A. Greco, and B. Keimer, "Gapped collective charge excitations and interlayer hopping in cuprate superconductors," Phys. Rev. Lett. **129**, 047001 (2022).

[34] Andrés Greco, Hiroyuki Yamase, and Matías Bejas, "Close inspection of plasmon excitations in cuprate superconductors," Phys. Rev. B **102**, 024509 (2020).

[35] Alexander L Fetter, "Electrodynamics of a layered electron gas. II. periodic array," Annals of Physics **88**, 1–25 (1974).

[36] A. Griffin and A. J. Pindor, "Plasmon dispersion relations and the induced electron interaction in oxide superconductors: Numerical results," Phys. Rev. B **39**, 11503–11514 (1989).

[37] Akira Iyo, Yasumoto Tanaka, Hijiri Kito, Yasuharu Kodama, Parasharam M. Shirage, Dilip D. Shivagan, Hirofumi Matsuhata, Kazuyasu Tokiwa, and Tsuneo Watanabe, "Tc vs n Relationship for Multilayered High-Tc Superconductors," Journal of the Physical Society of Japan **76**, 094711 (2007).

[38] M. Bejas, V. Zimmermann, D. Betto, T. D. Boyko, R. J. Green, T. Loew, N. B. Brookes, G. Cristiani, G. Logvenov, M. Minola, B. Keimer, H. Yamase, A. Greco, and M. Hepting,

"Plasmon dispersion in bilayer cuprate superconductors," Phys. Rev. B **109**, 144516 (2024).

[39] Hiroyuki Yamase, "Theory of charge dynamics in bilayer electron system with long-range coulomb interaction," Phys. Rev. B **111**, 085138 (2025).

[40] Niccolò Sellati and Lara Benfatto, "Ghost josephson plasmon in bilayer superconductors," Phys. Rev. B **111**, 104509 (2025).

[41] S. Nakata, M. Bejas, J. Okamoto, K. Yamamoto, D. Shiga, R. Takahashi, H. Y. Huang, H. Kumigashira, H. Wadati, J. Miyawaki, S. Ishida, H. Eisaki, A. Fujimori, A. Greco, H. Yamase, D. J. Huang, and H. Suzuki, "Out-of-phase plasmon excitations in the trilayer cuprate $Bi_2Sr_2Ca_2Cu_3O_{10+\delta}$," Phys. Rev. B **111**, 165141 (2025).

[42] M. Mitrano, A. A. Husain, S. Vig, A. Kogar, M. S. Rak, S. I. Rubeck, J. Schmalian, B. Uchoa, J. Schneeloch, R. Zhong, G. D. Gu, and P. Abbamonte, "Anomalous density fluctuations in a strange metal," Proc. Natl. Acad. Sci. U. S. A. **115**, 5392–5396 (2018).

[43] Aurelio Romero-Bermúdez, Alexander Krikun, Koenraad Schalm, and Jan Zaanen, "Anomalous attenuation of plasmons in strange metals and holography," Phys. Rev. B **99**, 235149 (2019).

[44] S. T. Van den Eede, T. J. N. van Stralen, C. F. J. Flipse, and H. T. C. Stoof, "Plasmons in a layered strange metal using the gauge-gravity duality," Phys. Rev. B **109**, 085119 (2024).

[45] H. Sun, M. Huo, X. Hu, J. Li, Z. Liu, Y. Han, L. Tang, Z. Mao, P. Yang, B. Wang, J. Cheng, D.-X. Yao, G.-M. Zhang, and M. Wang, "Signatures of superconductivity near 80 K in a nickelate under high pressure," Nature **621**, 493–498 (2023).

[46] J. Hou, P.-T. Yang, Z.-Y. Liu, J.-Y. Li, P.-F. Shan, L. Ma, G. Wang, N.-N. Wang, H.-Z. Guo, J.-P. Sun, Y. Uwatoko, M. Wang, G.-M. Zhang, B.-S. Wang, and J.-G. Cheng, "Emergence of High-Temperature Superconducting Phase in Pressurized La3Ni2O7 Crystals," Chinese Phys. Lett. **40**, 117302 (2023).

[47] Adriana Foussats and Andrés Greco, "Large-N expansion based on the Hubbard operator path integral representation and its application to the t-J model," Phys. Rev. B **65**, 195107 (2002).

[48] Abhishek Nag, M. Zhu, Matías Bejas, J. Li, H. C. Robarts, Hiroyuki Yamase, A. N. Petsch, D. Song, H. Eisaki, A. C. Walters, M. García-Fernández, Andrés Greco, S. M. Hayden, and Ke-Jin Zhou, "Detection of Acoustic Plasmons in Hole-Doped Lanthanum and Bismuth Cuprate Superconductors Using Resonant Inelastic X-Ray Scattering," Phys. Rev. Lett. **125**, 257002

(2020).

[49] Hiroyuki Yamase, "Theoretical insights into electronic nematic order, bond-charge orders, and plasmons in cuprate superconductors," J. Phys. Soc. Jpn. **90**, 111011 (2021).

[50] M. Hepting, T. D. Boyko, V. Zimmermann, M. Bejas, Y. E. Suyolcu, P. Puphal, R. J. Green, L. Zinni, J. Kim, D. Casa, M. H. Upton, D. Wong, C. Schulz, M. Bartkowiak, K. Habicht, E. Pomjakushina, G. Cristiani, G. Logvenov, M. Minola, H. Yamase, A. Greco, and B. Keimer, "Evolution of plasmon excitations across the phase diagram of the cuprate superconductor $La_{2-x}Sr_xCuO_4$," Phys. Rev. B **107**, 214516 (2023).

[51] Abhishek Nag, Luciano Zinni, Jaewon Choi, J. Li, Sijia Tu, A. C. Walters, S. Agrestini, S. M. Hayden, Matías Bejas, Zefeng Lin, H. Yamase, Kui Jin, M. García-Fernández, J. Fink, Andrés Greco, and Ke-Jin Zhou, "Impact of electron correlations on two-particle charge response in electron- and hole-doped cuprates," Phys. Rev. Res. **6**, 043184 (2024).

[52] Matías Bejas, Xianxin Wu, Debmalya Chakraborty, Andreas P. Schnyder, and Andrés Greco, "Out-of-plane bond-order phase, superconductivity, and their competition in the t-$J_\parallel$-$J_\perp$ model: Possible implications for bilayer nickelates," Phys. Rev. B **111**, 144514 (2025).

[53] P. Prelovšek and P. Horsch, "Electron-energy loss spectra and plasmon resonance in cuprates," Phys. Rev. B **60**, R3735–R3738 (1999).

[54] (), in reality, one would expect $J_\perp/J \sim 0.1$ [65, 66], yielding $J_\perp/t \sim 0.03$, which, however, may be small enough to be neglected.

[55] Matías Bejas, Andrés Greco, and Hiroyuki Yamase, "Possible charge instabilities in two-dimensional doped Mott insulators," Phys. Rev. B **86**, 224509 (2012).

[56] Matías Bejas, Andrés Greco, and Hiroyuki Yamase, "Strong particle-hole asymmetry of charge instabilities in doped Mott insulators," New J. Phys. **16**, 123002 (2014).

[57] J. Hubbard, "Electron correlations in narrow energy bands," Proc. R. Soc. Lond. A **276**, 238–257 (1963).

[58] L. Faddeev and R. Jackiw, "Hamiltonian reduction of unconstrained and constrained systems," Phys. Rev. Lett. **60**, 1692–1694 (1988).

[59] K. Sundermeyer, *Constrained Dynamics* (Berlin: Springer, 1982).

[60] Jan Govaerts, "Hamiltonian reduction of first-order actions," Int. J. Mod. Phys. A **05**, 3625–3640 (1990).

[61] Adriana Foussats and Andrés Greco, "Large-N expansion based on the Hubbard operator

path integral representation and its application to the $t-J$ model. II. The case for finite J," Phys. Rev. B **70**, 205123 (2004).

[62] Hiroyuki Yamase, Matías Bejas, and Andrés Greco, "Electron self-energy from quantum charge fluctuations in the layered $t - J$ model with long-range Coulomb interaction," Phys. Rev. B **104**, 045141 (2021).

[63] Matías Bejas, Hiroyuki Yamase, and Andrés Greco, "Dual structure in the charge excitation spectrum of electron-doped cuprates," Phys. Rev. B **96**, 214513 (2017).

[64] J. M. Tranquada, B. J. Sternlieb, J. D. Axe, Y. Nakamura, and S. Uchida, "Evidence for stripe correlations of spins and holes in copper oxide superconductors," Nature **375**, 561–563 (1995).

[65] S. M. Hayden, G. Aeppli, T. G. Perring, H. A. Mook, and F. Doğan, "High-frequency spin waves in $YBa_2Cu_3O_{6.15}$," Phys. Rev. B **54**, R6905–R6908 (1996).

[66] D. Reznik, P. Bourges, H. F. Fong, L. P. Regnault, J. Bossy, C. Vettier, D. L. Milius, I. A. Aksay, and B. Keimer, "Direct observation of optical magnons in $YBa_2Cu_3O_{6.2}$," Phys. Rev. B **53**, R14741–R14744 (1996).